Development of Advanced Silicon Radiation Detectors for High Energy Physics and Medical Imaging

Master Thesis
Juan Pablo Balbuena Valenzuela

UAB
Universitat Autònoma de Barcelona

CNM
Centre Nacional de Microelectrònica IMB

Contents

Abstract

The 1st chapter of this work presents the different experiments and collaborations in which I am involved during my PhD studies of Physics. Following those descriptions, the 2nd chapter is dedicated to how the radiation affects the silicon sensors, as well as some experimental measurements carried out at CERN (Geneve, Schwitzerland) and IFIC (Valencia, Spain) laboratories. Besides the previous investigation results, this chapter includes the most recent scientific papers appeared in the latest RD50 (Research & Development #50) Status Report, published in January 2007, as well as some others published this year.

The 3rd and 4th are dedicated to the simulation of the electrical behavior of solid state detectors. In chapter 3 are reported the results obtained for the illumination of edgeless detectors irradiated at different fluences, in the framework of the TOSTER Collaboration. The 4th chapter reports about simulation design, simulation and fabrication of a novel 3D detector developed at CNM for ions detection in the future ITER fusion reactor. This chapter will be extended with irradiation simulations and experimental measurements in my PhD Thesis.

1 Introduction

This chapter presents a short introduction about the projects I have been involved during my research work.

1. CERN RD50 collaboration [1], that continues the work of RD48 (for LHC) [2][3], but this time for S-LHC, in the research and development of new semiconductor detectors able to work correctly under hard radiation environments. These advances will be used for the upgrade of the current ATLAS detector, called ATLAS Upgrade.

2. Total Cross Section, Elastic Scattering and Diffraction Dissociation at the LHC (TOTEM) [4][5], which is an experiment dedicated to the measurement of total cross section, elastic scattering and diffractive processes between the protons in the beam at the LHC. Edgeless detectors have been placed as close as possible of the beam to detect scattered protons but not interacting with the beam.

3. International Thermonuclear Experimental Reactor (ITER) [6], this experiment has the aim to demonstrate the scientific and technological feasibility of fusion power for peaceful purposes.

1.1 Experiments in High Energy Physics: LHC

1.1.1 Description

The Large Hadron Collider (LHC) [2] is a huge particle accelerator and collider located at CERN, near Geneva, Switzerland. This accelerator is expected to start to work on spring 2009. The LHC is being funded and built in collaboration with hundreds of physicists from thirty-four countries, universities and institutes.

The collider is contained in a 27 km circumference tunnel located underground at a depth ranging from 50 to 175 m. The tunnel was formerly used to house the LEP, an electron-positron collider. The collider tunnel contains two pipes enclosed within superconducting magnets cooled by liquid helium, each pipe containing a proton beam. The two beams travel in opposite directions around the ring. Additional magnets are used to direct the beams to four intersection points where interactions between them will take place.

The protons will have an energy of 7 TeV, giving a total collision energy of 14 TeV in the center of mass. It will take around 90 microseconds for an individual proton to travel once around the collider. Beams of lead nuclei will be also accelerated, smashing together with a collision energy of 1150 TeV. Rather than continuous beams, the protons will be "bunched" together into approximately 2,800 bunches, so that interactions between the two beams will take place at discrete intervals never shorter than twenty-five nanoseconds apart. When the collider is first commissioned, it will be operated with fewer bunches, to give a bunch crossing interval of seventy-five nanoseconds. The number of bunches will later be increased to give a final bunch crossing interval of twenty-five nanoseconds.

Prior to being injected into the main accelerator, the particles are prepared through a series of systems that successively increase the particle energy levels. The first system is the linear accelerator Linac2 generating 50 MeV protons which feeds the Proton Synchrotron Booster (PSB). Protons are then injected at 1.4 GeV into the Proton Synchrotron (PS) at 26 GeV. The Low-Energy Injector Ring (LEIR) will be used as an ion storage and cooler unit. The Antiproton Decelerator (AD) will produce a beam of anti-protons at 2 GeV, after cooling them down from 3.57 GeV. Finally the Super Proton Synchrotron (SPS) can be used to increase the energy of protons up to 450 GeV.

Six detectors are being constructed at the LHC. They are located underground, in large caverns excavated at the LHC's intersection points. Two of them, ATLAS and CMS are large, "general purpose" particle detectors. The other four (LHCb, ALICE, TOTEM, and LHCf) are smaller and more specialized. A scheme of the different experiments in LHC are shown in Figure 1.1.

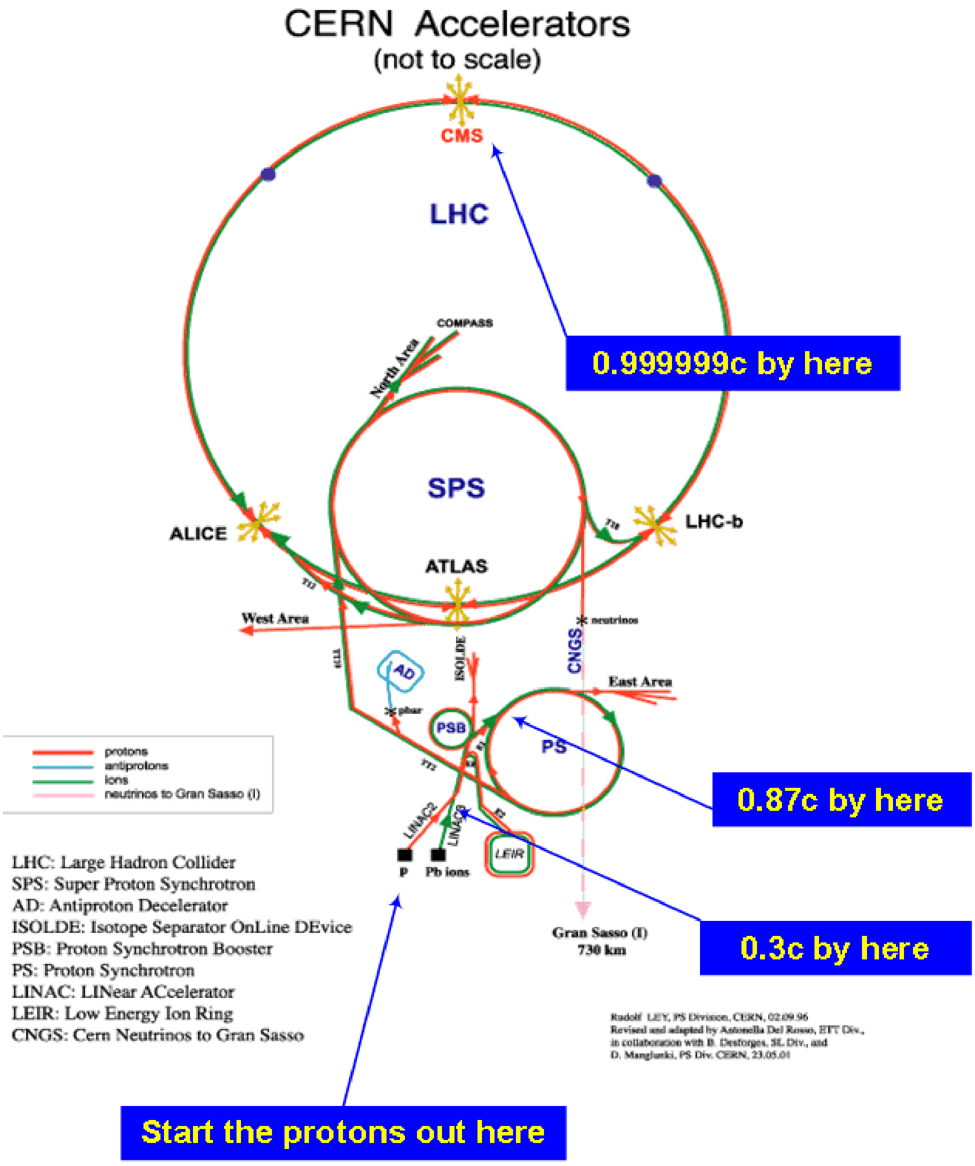

0.999999c by here

0.87c by here

0.3c by here

Start the protons out here

Figure 1.1: *Schema of CERN complex at Geneve.*

1.1.2 Motivation and objectives

The main reason for LHC building is to increase the understanding of the fundamental structure of the universe. We have seen that the theory we use, the Standard Model, leaves many unsolved questions. Among them, the reason why elementary particles have mass, and why their masses are different is the most perplexing one. It is remarkable that such a familiar concept is so poorly understood.

The answer may lie within the Standard Model in an idea named the Higgs mechanism. According to this hypothesis, the whole of space is filled with a 'Higgs field', and by interacting with this field, particles acquire their masses. Particles which interact strongly with the Higgs field are heavy, whilst those which interact weakly are light. The Higgs field has at least one new particle associated with it, the Higgs boson. If such particle exists, the LHC will be able to make it detectable.

And, what about the four forces? When the Universe was young and much hotter than today, perhaps these forces all behaved as one. Particle physicists hope to find a single theoretical framework to prove this, and have already had some success. Two forces, the electromagnetic force and the weak force were 'unified' into a single theory in the 1970s. This theory was experimentally verified in a Nobel prize winning experiment at CERN a few years later. The weakest and the strongest forces, however, gravity and the strong force, remain apart.

A very popular idea suggested by the unification of the forces is called supersymmetry, or SUSY for short. SUSY predicts that for each known particle there is a 'supersymmetric' partner. If SUSY is right, then supersymmetric particles should be found at the LHC.

The LHC might also shed some light on other cosmological questions such as dark energy, dark matter, extra dimensions and the riddle of antimatter.

In physical cosmology, dark energy is a hypothetical form of energy that permeates all of space and tends to increase the rate of expansion of the universe. Assuming the existence of dark energy is the most popular way to explain recent observations that the universe appears to be expanding at an accelerating rate. In the standard model of cosmology, dark energy currently accounts for almost three-quarters of the total mass-energy of the universe.

Two proposed forms for dark energy are the cosmological constant, a constant energy density filling space homogeneously, and quintessence, a dynamic field whose energy density can vary in time and space. Distinguishing between the alternatives requires high-precision measurements of the expansion of the universe to understand how the speed of the expansion changes over time. The rate of expansion is parameterized by the cosmological equation of state. Measuring the equation of state of dark energy is one of the biggest efforts in observational cosmology today.

Adding the cosmological constant to cosmology's standard FLRW metric leads to the Lambda-CDM model, which has been referred to as the "standard model" of cosmology because of its precise agreement with observations.

There are many reasons to believe that the universe is full of "dark matter", matter that influences the evolution of the universe gravitationally, but is not seen directly in our present observations. That presence of “missing mass” can be detected through microlensing and X-Ray images of galaxies as in Figures 1.2 and 1.3. The nature of this dark matter is one of the fundamental cosmological issues of modern astrophysics. The composition of dark matter is unknown, but may include ordinary and heavy neutrinos, recently postulated elementary particles such as WIMPs and axions, astronomical bodies such as dwarf stars and planets (collectively called MACHOs), and clouds of non-luminous gas. Current evidence favors models in which the primary component of dark matter is new elementary particles, collectively called non-baryonic dark matter.

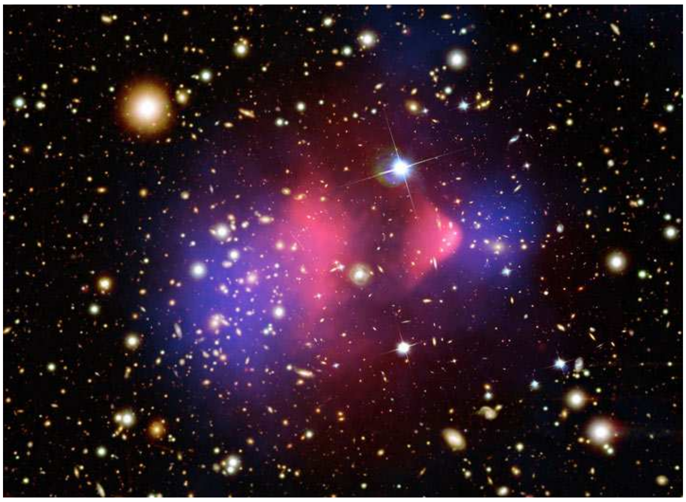

Figure 1.2: *Superposition of visible (white) and X-Ray images (red and blue) of a cluster of galaxies.*

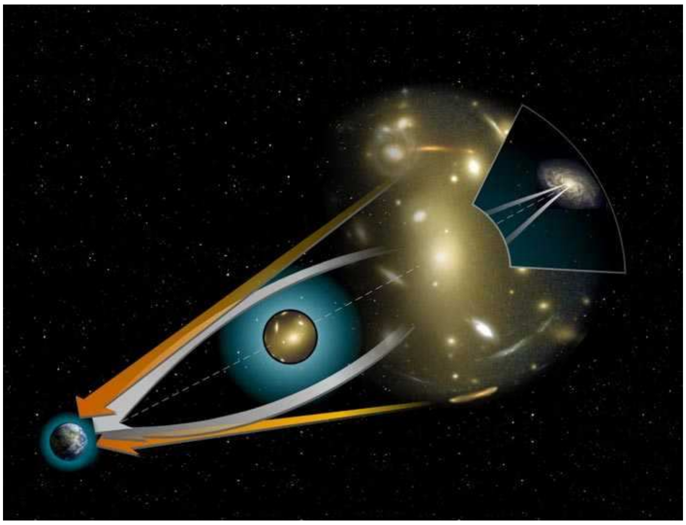

Figure 1.3: *This picture shows the functioning of gravitational lensing.*

Our world has very known 3+1 dimensions, 3 spatial dimensions and the forth is the time. While time is very different from the familiar spatial dimensions, Lorentz and Einstein showed at the beginning of the 20th century that space and time are intrinsically related. The idea of additional spatial dimensions comes from string theory, the only self-consistent quantum theory of gravity so far. It turns out that for a consistent description of gravity, one needs more than 3+1 dimensions, and the world around us could have up to 11 spatial dimensions. These extra spatial dimensions, if they really exist, are thought to be curled-up or compactified. LHC should be able to probe the theory of large extra dimensions and either find them or show that the idea is actually wrong.

It was once thought that antimatter was a perfect 'reflection' of matter - that if you replaced matter with antimatter and looked at the result in a mirror, you would not be able to tell the difference. We now know that the reflection is imperfect, and this could have led to the matter-antimatter imbalance.

The LHC will be a very good 'antimatter-mirror', allowing us to put the Standard Model through one of its most gruelling tests yet.

These are just a few of the questions the LHC should answer, but history has shown that the greatest advances in science are often unexpected. Although we have a good idea of what we hope to find at the LHC, nature may well have surprises in store. One thing is certain, the LHC will change our view of the Universe.

1.1.3 Procedure of functioning

The way of having these particle beams perfectly collided is by using superconductivity. To keep the LHC's beams on track needs stronger magnetic fields than have ever been used before in a CERN accelerator [7].

Superconductivity makes such fields possible, but a superconducting installation as large as the LHC has never before been built. Intensive R&D with European industry has shown that it can be done. At the end of 1994, an important milestone was reached with the first operation of an entire prototype section of the accelerator.

Superconductivity is the ability of certain materials to conduct electricity without resistance or energy loss, usually at very low temperatures. The LHC will operate at about 300 degrees below room temperature (1.9 K), even colder than outer space.

Because the LHC will accelerate two beams moving in opposite directions, it is really two accelerators in one. To keep the machine as compact and economical as possible, the magnets for both will be built into a single 2-in-1 housing. The beams move around the LHC ring inside a continuous vaccum guided by magnets. There are many types of magents used in LHC although the biggest are the main dipoles, Figure 1.4.

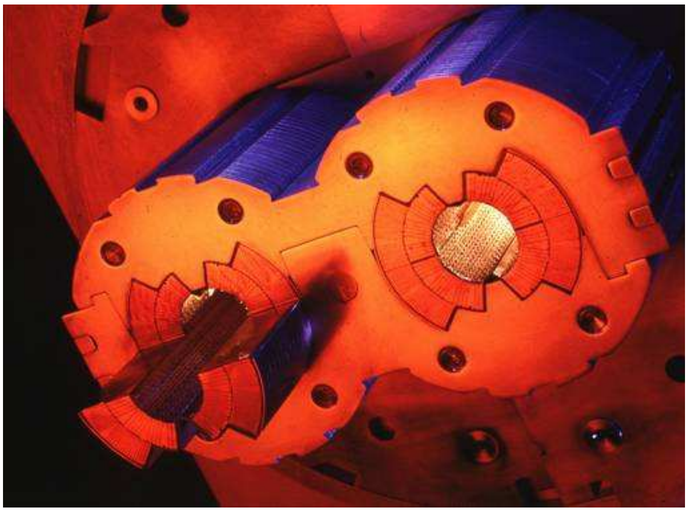

Figure 1.4: *Close look of one of the main dipoles.*

At 7 TeV these magnets have two apertures, one for each of the counter-rotating beams. Each one is 14.3 metres long. A total of 1232 are needed. These superconducting dipoles produce a field of 8.4 T.

The LHC will be built in the same tunnel as CERN's Large Electron Positron collider, LEP, and so will cost much less than a similar machine on a green field site. Proton beams will be prepared by CERN's existing accelerator chain before being injected into the LHC. Each proton beam at full energy will consist of 2808 bunches per beam, and each bunch will contain 1.15×10^{11} protons at the start of nominal fill.

The particles in the LHC are ultra-relativistic and move at 0.999997828 times the speed of light at injection and 0.999999991 the speed of light at top energy. So total beam energy at top energy is

$$2808\ bunches \times 1.15{\cdot}10^{11}\ protons\ @\ 7TeV = \qquad \mathbf{362\ MJ}$$

1.1.4 Large Hadron Collider (LHC)

The Large Hadron Collider (LHC) at CERN was scheduled to be operational in year 2009. Although the LHC is not yet in function, studies on the physics potential and the experimental challenges for an upgrade of the LHC to a 10 times higher luminosity of 10^{35} cm^{-2}s^{-1} have been performed for the accelerator and the experiments. A clear gain in physics potential has been identified but also the urgent need for setting up as soon as possible an intensive R&D program for both, in order to match the more stringent and very challenging requirements of Super-LHC.

The luminosity of the colliding is formulated as follows

$$L = \frac{N_b^2 n_b f_0}{4\pi\varepsilon\beta^*} \qquad (1)$$

for a circular cross-section beam with head-on collisions, where N_b is the number of particles in a bunch, n_b, is the number of bunches, and β^* is the beta function defending the transverse beam size at IR.

The increase of luminosity by a factor of 10 can be achieved with three factors. By increasing the N_b to an ultimate value of 1.7×10^{11} protons per bunch, limited by beam-beam limit, from the nominal value of 1.1×10^{11}, the luminosity can be increased to 2.3×10^{34} cm^{-2}s^{-1}. By reducing the beta function, β^*, to 0.25m from the nominal of 0.5m by modifying the IR-Q magnets and/or IR layouts, the luminosity can be increased to 4.6×10^{34} cm^{-2}s^{-1}. By doubling the number of bunches, n_b, to 5616 bunches from nominal 2808, the luminosity can be increased to 9.2×10^{34} cm^{-2}s^{-1}. Doubling the numbers of bunches means reducing the bunch spacing to 12.5ns from the nominal value of 25ns. This requires upgrading cryogenics, collimation, the dumping system, and possibly upgrading the RF system in the super-proton synchrotron (SPS) and modifications to the injectors.

For the second stage of the Super-LHC upgrade we have that the beam intensity and brilliance can be increased by a factor of 2 beyond its nominal ultimate value by upgrading the SPS with superconducting magnets and upgrading the transfer lines, thus injecting protons into the LHC at 1 TeV and reducing the energy swing by a factor of 2. By upgrading the LHC with new dipole magnets with a field of 15 T, the beam energy cab be increased to 12.5 TeV. The stage-2 Super-LHC would be operating by 2020.

1.1.4.1 ATLAS Upgrade

A Toroidal LHC ApparatuS, (ATLAS) [8], Figure 1.5, is a particle physics experiment that will explore the fundamental nature of matter and the basic forces that shape our universe. The ATLAS detector will search for new discoveries in the head-on collisions of protons of extraordinarily high energy. ATLAS is one of the largest collaborative efforts ever attempted in the physical sciences. There are 2100 physicists (Including 450 students) participating from more than 167 universities and laboratories in 37 countries.

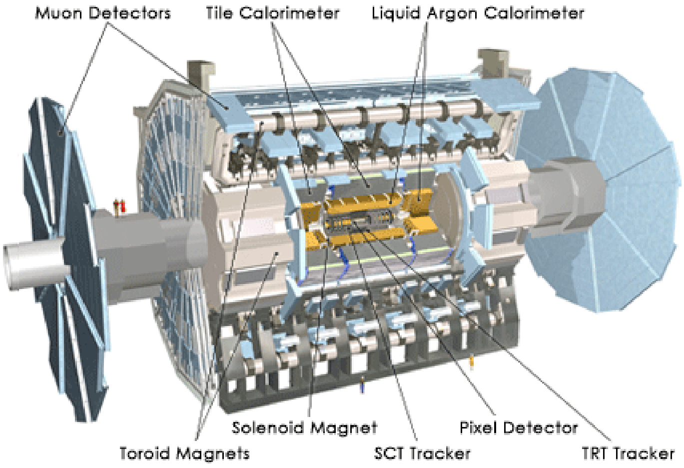

Figure 1.5: *Design of the ATLAS detector at CERN.*

When LHC has its fluence increased the semiconductor sensors located in the inner detector could not support that hard radiation environment and will be replaced by which result from RD50 collaboration developments. The experiment to carry out that goal is called ATLAS Upgrade [9].

1.1.4.2 The TOTEM experiment

The TOTEM Experiment [5], Figure 1.6, is aimed to obtain accurate information on the basic properties of proton-proton collisions at the maximum accelerator energy. For these measurements it is needed to detect particles emitted in the very forward region. To carry out this work, TOTEM will measure the total *pp* cross-section scattering with an accuracy of the order of 1%, which is sufficient to discriminate between the current model predictions for the LHC energy ranging between 100 and 130 mb, and also will study elastic scattering and diffractive dissociation at LHC. The measurement of elastic *pp* scattering down to the four-momentum transfer squared $-t = 10^{-3}$ GeV^2 is accomplished by silicon detectors placed in Roman Pots located at 147m and 220m from IP5. The beam of the LHC being rather thin, with a 10σ envelope of about 1mm, the detectors in the Roman Pot must have a very small dead zone at the mechanical edge facing the beam. TOTEM will also measure *pp* scattering up to –t ~ 10 GeV^2.

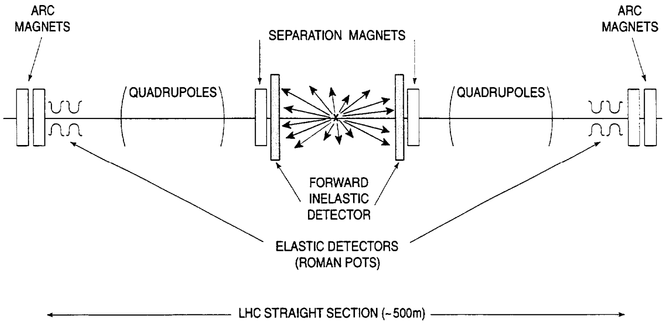

Figure 1.6: *Sketch of the experimental apparatus of TOTEM.*

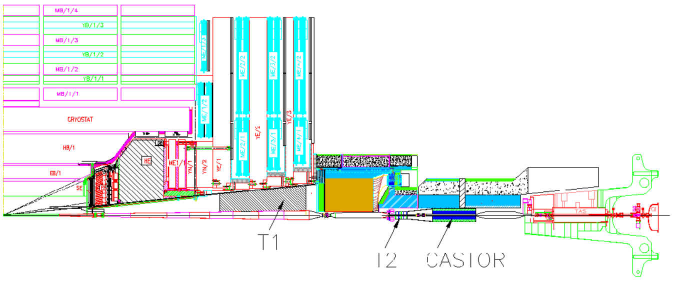

Figure 1.7: *The TOTEM detectors T1 and T2 installed in the CMS forward region.*

Given the large cross-sections involved, the experiment does not require intense beams, but a special high-beta optics is needed for the measurement of low t elastic scattering. The experiment will be ready to take data at the beginning of the LHC operation and will also provide an absolute luminosity determination.

The TOTEM experiment uses precision detectors inserted in Roman Pots and/or microstation installed in the machine tunnel to measure the elastically and diffractively scattered protons close to the beam directions. Two separate forward telescopes (T1 and T2) will be installed on both sides of the CMS detector, Figure 1.7, with a rapidly coverage of $3 \leq \eta \leq 6.8$. With these additional detectors, a fully inclusive trigger, also for the single diffraction, can be provided with an expected loss on the inelastic rate of less than 2%.

The elastic and inelastic interaction rates are related to the integrated luminosity of the machine by the equation:

$$L\sigma_{tot} = N_{el} + N_{inel} \tag{2}$$

The optical theorem relates the total cross-section to the imaginary part of the forward scattering amplitude leading to the following equations:

$$L\sigma_{tot}^2 = \frac{16\pi}{1+\rho^2}\left(\frac{dN}{dt}\right)_{t=0} \tag{3}$$

Combining both equations we can write the total cross-section as a function of measurable quantities:

$$\sigma_{tot} = \frac{16\pi}{1+\rho^2}\frac{(dN/dt)_{t=0}}{N_{el}+N_{inel}} \tag{4}$$

Solving previous equations for L shows that TOTEM will also be able to provide an absolute calibration of the machine luminosity. The ρ parameter with its small value at high energies (0.1 – 0.2) does not significantly influence the final precision of the measurement.

TOTEM only needs few one day runs, with the special running conditions of a high $\beta^*\sim1500$ m, a reduced number of bunches, a low luminosity of $L \approx 10^{28}$ $\text{cm}^{-2}\text{s}^{-1}$, and a beam crossing-angle of zero degrees. This is sufficient to collect an integrated luminosity of typically 10^{33} cm^{-2} which correspond to $10^7 - 10^8$ minimum bias events.

Almost half of the total cross-section at the LHC is predicted to be due to the coherent elastic scattering, single, double and central diffractive processes.

At $\beta^*\sim1500$ m, the TOTEM experiment efficiency detects protons with $-t > 0.004$ GeV^2, i.e. 97% of all the diffractively scattered protons, independent of their longitudinal momentum loss in the range of $10^{-8} < \Delta p/p < 0.2$. With the TOTEM acceptance extending up to the pseudorapidities of 6.8, and with the efficient proton detection capabilities close to the LHC beams, it is only the diffractively excited states with masses below 4 GeV/c^2 that are missed by the experiment.

For non-diffractive inclusive events, a substantial fraction of the total energy is detected. In order to extend the acceptance further (to cover new phenomena such as coherent pion production) additional detectors close to the beam and before the first limiting aperture of the LHC could be installed. Very forward neutral particles are detected in the zero-degree calorimeters that equip the region where the two beams separate. In summary, it will be possible to study particle production over the entire phase space during low luminosity runs.

Roman Pots

The leading proton detectors are installed into special beam pipe insertions called Roman Pots [10], shown in Figures 1.8, 1.10 and 1.11. The detector systems have to fulfill stringent requirements set by the LHC machine and the TOTEM experiment. The high intensity proton bunches pose a challenge concerning possible pick-up in the detectors close to the LHC beams. The detector systems have to be robust, aligned to within 20μm and their positions accurately maintained. Moreover, the detector systems have to withstand in the high-radiation environment of the LHC.

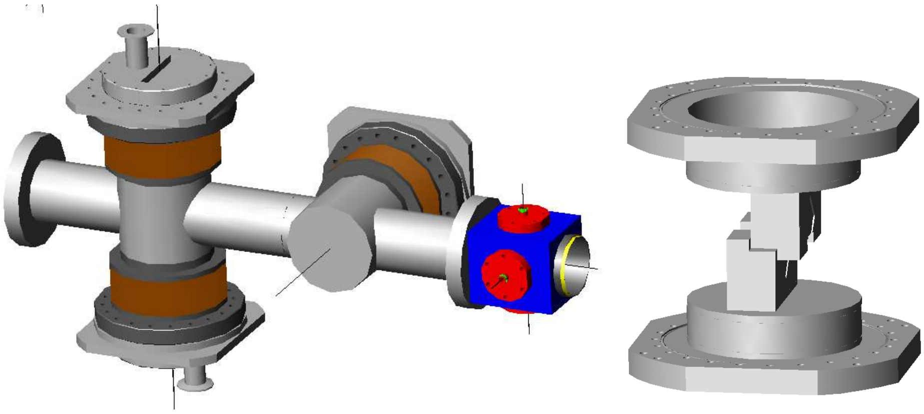

Figure 1.8: *Roman Pot unit (right) and detail of vertical setup (left).*

During operation the detector edge is positioned at a distance of less than 1 mm from the axis of the high intensity proton beam where a 200 µm window separates the detectors from the primary beam vacuum, Figure 1.9. For optimal performance, the detector has to approach the envelope of the beam as closely as possible. Consequently, the detectors should be active up to their physical edge. It is our aim that the active volume should be within 50 µm of the edge. In general, planar silicon detectors have a wide (0.5 – 1 mm) insensitive border region around the sensitive area. This insensitive region is occupied by a sequence of guard rings which controls the potential distribution between the detector's sensitive area and the die cut to minimize the electrical field and, thus, the surface leakage current.

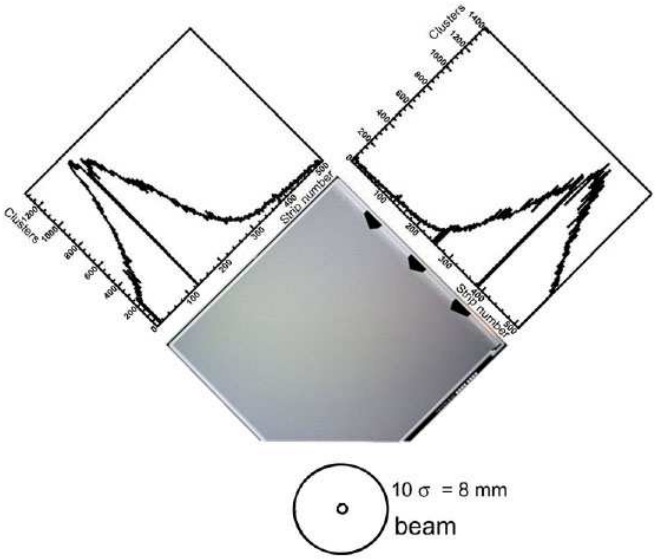

Figure 1.9: *Tracks response of edgeless detector.*

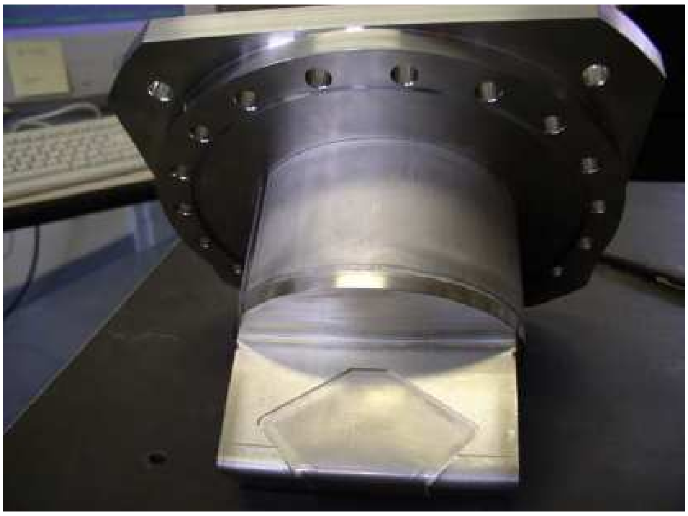

Figure 1.10: *Picture of the pot with the thin window.*

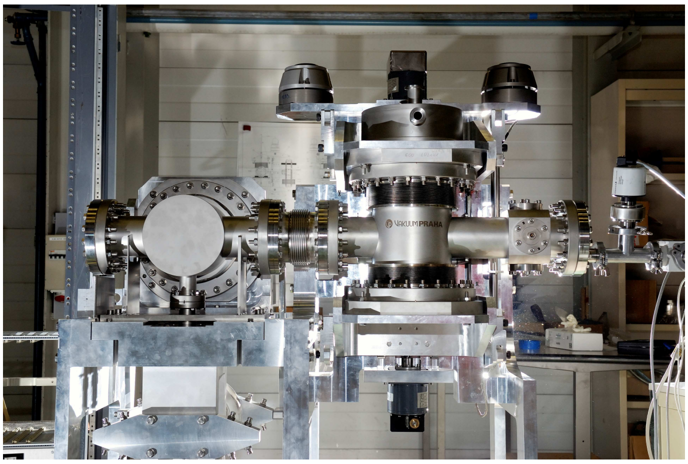

Figure 1.11: *Assembled Roman Pot.*

At both locations 147 m and 220 m, two Roman Pot stations separated by a distance of several meters will permit a precise determination of the angle, even on the trigger level, thus reducing the background due to beam-gas and halo interactions, Figure 1.12. It is important to note that the 147 m Roman pots are located before the D2 magnet, while the 220 m tracking station is well behind it. This geometry naturally implements a magnetic spectrometer in the standard insertion, permitting TOTEM to measure particle momenta, with an accuracy of a few parts per thousand. This will allow the accurate determination of the momentum loss of quasi-elastically scattered protons in diffractive processes.

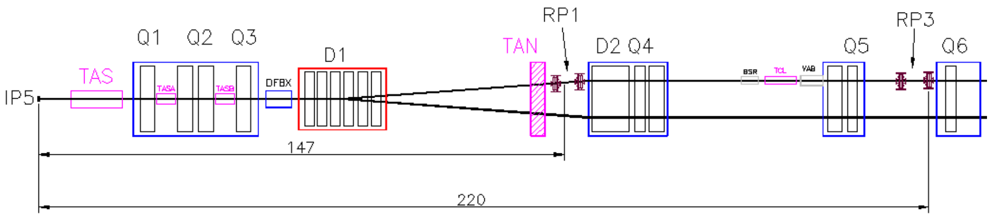

Figure 1. 12: *The LHC line with Roman Pots at 147 m and 220 m.*

1.2 Other Applications: The ITER project

The ITER project [6] has the aim to demonstrate the scientific and technological feasibility of fusion power for peaceful purposes. It will be placed in Cadarache, in the south of France.

ITER is a tokamak, in which strong magnetic fields confine a torus-shaped fusion plasma. This plasma consists of deuterium and tritium at high temperature. This temperature generated by the fusion process is supposed to be higher than needed to keep deuterium and tritium in plasma state. So there is an excess of thermal energy which can be handled to generate electrical power. Compared with current conceptual designs for future fusion power plants, ITER will include most of the necessary technology, but will be of slightly smaller dimensions and will operate at about one-sixth of the power output level.

JET, presently the largest tokamak in the world, has reached Q = 0.65 (Q is the represents the amount of thermal energy that is generated by the fusion reactions, divided by the amount of external heating), near the point of "break even" (Q=1). ITER has to be able to produce Q=10, or Q larger than 5 when pulses are stretched towards a steady state.

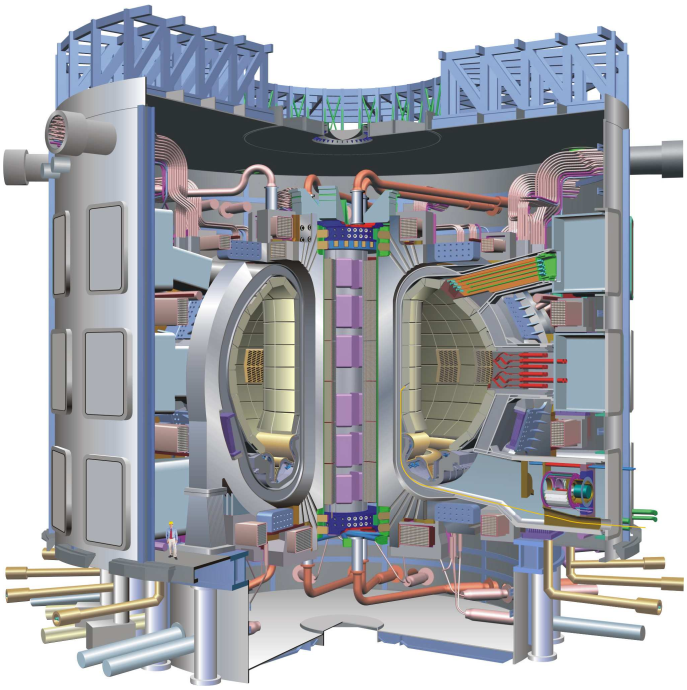

Figure 1.13: *Design of the ITER machine.*

For these purposes, ITER should implement and test the key technologies and processes needed for future fusion power plants - including superconducting magnets, components able to withstand high heat loads, and remote handling. Also should test and develop concepts for breeding tritium from lithium-containing materials inside thermally efficient high temperature blankets surrounding the plasma.

The steps beyond ITER are open at this stage. During the ITER construction and operation period, other magnetic confinement schemes or inertial fusion may show more promising than ITER, so the door is open for these schemes to supersede the tokamak in subsequent steps. Certainly, the technologies developed for and tested on ITER: remote maintenance, tritium breeding high temperature blankets, and high heat flux components, will provide essential information whatever the confinement scheme used.

New semiconductor sensors have to be developed for the high quantity of neutrons in this environment. The task of these sensors is monitoring the plasma temperature by analyzing particles that escape from it. For this purpose, RD50 technology in radiation hardness can be used, but taking into account that high radiation dose in ITER is higher than in the inner detector of ATLAS Upgrade. In this way 3D detector can be developed using p-type substrate (more resistant to radiation) due to the electron read out, but not-oxygenated, because in neutron irradiation V_2O production within the cluster appears to dominate at all fluences, independent of oxygen concentration [14].

2 Radiation hard detectors

The envisaged upgrade of the Large Hadron Collider (LHC) at CERN towards the Super-LHC (SLHC) with a 10 times increased luminosity of 10^{35} cm^{-2} s^{-1} will present severe challenges for the tracking detectors of the SLHC experiments. Unprecedented high radiation levels and track densities and a reduced bunch crossing time in the order of 25 ns as well as the need for cost effective detectors have called for an intensive R&D program.

The CERN RD50 collaboration "Development of Radiation Hard Semiconductor Devices for Very High Luminosity Colliders" is working on the development of semiconductor sensors matching the requirements of the SLHC. Sensors based on defect engineered silicon like Magnetic Czochralski, epitaxial and oxygen enriched silicon have been developed. With 3D, Semi-3D and thin detectors new detector concepts have been evaluated and a study on the use of standard and oxygen enriched p-type silicon detectors revealed a promising approach for radiation tolerant cost effective devices [11].

The detectors of this study are silicon microstrips detectors (Figure 2.1), fabricated at CNM using different types of silicon materials: FZ (Float Zone), DOFZ (Diffusion Oxygenated Float Zone), EPI (Epitaxial) and MCZ (Magnetic Czochraslki) for p-type, FZ for n-in-n type, and EPI and MCZ for n-type. The results of the electrical measurements of these detectors are reported in this chapter.

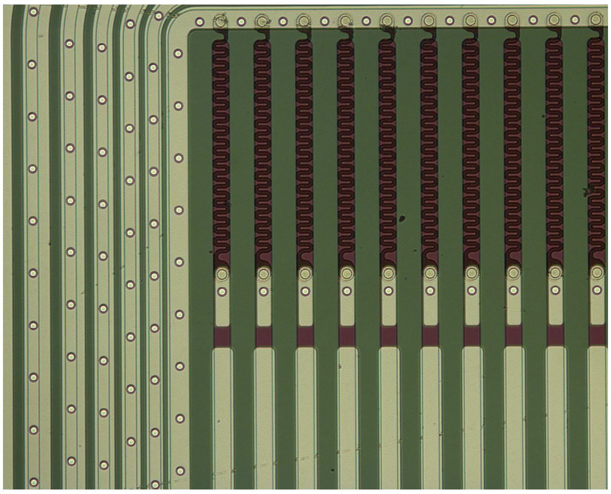

Figure 2.1: *Picture of one N-on-P microstrips detector fabricated using RD50 collaboration's masks.*

2.1 Silicon radiation detectors

An intrinsic semiconductor is defined as the material which has all of its atoms of the same type, in other words, without impurities.

Semiconductors which are modified with impurities are called doped. These impurities consist of a small quantity of different atoms and so we get an extrinsic semiconductor. This way it is possible to increase the conductivity due to the energy levels that are created in the forbidden gap.

When silicon is doped using atoms of the fifth group (P,As,…) these atoms take up the place of the silicon atoms of the crystalline net. Each atom has five electrons in the valence band, four of them take part in the covalent links with its close silicon atoms. The remaining electron is weakly linked to its nuclei and will require a much smaller energy than E_{gap} to jump to the conduction band. This way it is possible to add electrons to the conduction band, leaving behind a positively simple-ionized fixed atom at room temperature. Electrons are the majority carriers and holes are called minority carriers. This kind of impurities are named donor impurities and the extrinsic semiconductor will be n-type.

On the other hand, if we dope the silicon using atoms of the third group (B,Al,…), which only have 3 electrons in the valence band, holes are being introduced in the net which are easily excitable to reach the valence, leaving behind a negatively simple-ionized fixed atom at room temperature. In this case, the majority carriers are holes and the electrons are called minority carriers. These kinds of impurities are named acceptor impurities and the extrinsic semiconductor will be p-type [12].

2.1.1 Radiation damage in silicon detectors

Electronic devices are affected by radiation through several ways. The first type of damage takes place in the bulk due to Non Ionizing Energy Loss (NIEL). This effect consists of the displacement of the atoms of silicon from their locations in the lattice and the resulting defects modify the electronic properties of the crystal structure. The second type is the Ionizing energy Loss (IEL) damage, which takes place in the outer layer (surface of the detector) affecting oxides (SiO_2), in which charge carriers generated by ionization can move by drift of diffusion and are trapped in other places, generating charge concentrations which produce parasitic fields. Besides, it can take place nuclear transmutations by neutron capture, in particular if radiation is composed by slow neutrons. The bulk and surface damage will be discussed in detail since are the main responsible for the degradation of Silicon detectors.

The ionizing effects depend fundamentally on the total absorbed energy and independent of the type of radiation. However, the produced ionization is material dependant, because it depends on the number of electron-hole pairs created by absorbed energy unit, which is measured in rad or Gy.

Because of this, we have to talk in terms of absorbed ionizing radiation dose in each material.

On the other hand, displacement damage is function of the type of radiation because it depends on the quantity of energy and momentum transferred to the nuclei in the lattice, which are mass and energy dependent. For this reason, displacement damage must be specified for each particle and energy.

- **Bulk (crystal) damage due to Non Ionizing Energy Loss (NIEL)**

Displacement damage is the consequence of a non ionizing particle interaction of an impinging particle ($\beta^{+/-}$, p, n, ions, γ-rays) with the lattice atoms. The collision between the particle and the nucleus displaces the nucleus from its position in the lattice, producing point defects known as *Frenkel pairs*, which consist of one interstitial atom and a vacancy. Most of these defects are not stable. Interstitials and vacancies are mobile at room temperature and will therefore partially anneal if by chance an interstitial fills the place of a vacancy. However, it is also possible the formation of other (room temperature) stable defects.

The minimum ionizing energy needed to displace one silicon atom is around 15eV, although it depends on the backscattering direction. From the point of view of probabilities, if the impinging particle transfers an energy greater than 25eV to the silicon atom one Frenkel pair will be created, while for lower energies occurs the dissipation of the energy via lattice vibrations [13].

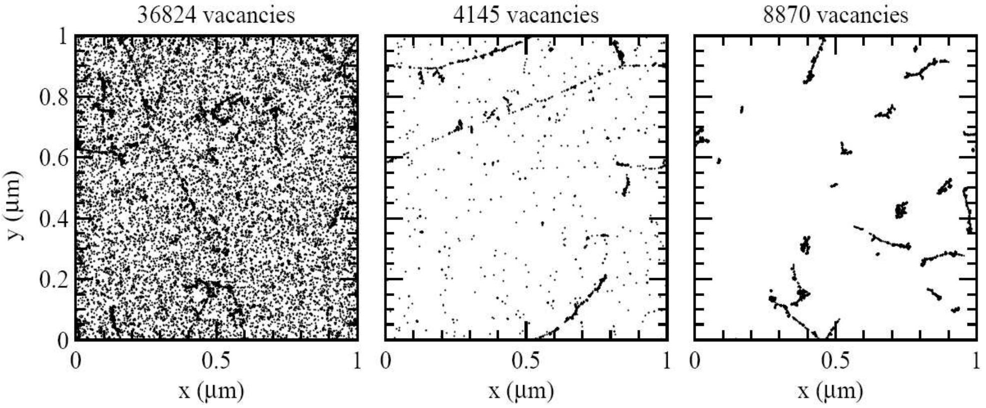

Figure 2.2: *Initial distribution of vacancies produced by 10 MeV protons (left), 24 GeV protons (middle) and 1 MeV neutrons (right). The plots are projections over 1 μm of depth (z) and correspond to a fluence of*10^{14} cm^{-2}*[14].*

The Primary Knock-on Atom (PKA), in its movement is able to generate another point defects or high density groups, known as clusters, depending on the energy transferred in the collision. An atom of silicon with backscattering energy of 1-2 keV only produces point defects; with 2-12 keV it is able to produce a cluster and several point defects, and with higher energies than 12 keV it will create some clusters [13]. Clusters appears at the end of the silicon atom track, where it losses its last keVs of energy and the cross section for the elastic collision is increased several orders of magnitude.

It is proven that the damage in silicon created by the impinging particle is generally proportional to the non ionizing energy loss (NIEL), which is the energy that the particle leaves per unit length in its interaction with the nuclei of the lattice [15]. This behavior can be expressed by the so-called displacement damage cross-section *D*. This quantity is equivalent to the NIEL [16] and hence the proportionality between the NIEL value and the resulting damage. *D* is normally quantified in MeV·mb, while NIEL is given in keV·cm^2/g. For silicon with atomic mass A = 28.086 g/mol the relation between *D* and NIEL is 100 MeV mb = 2.144 keV·cm^2/g. According to an ASTM standard, the displacement damage cross section for 1 MeV neutrons is set as a normalizing value: D_n(1 MeV) = 95 MeV·mb [17]. NIEL value is depending on the particle type and energy and can be scaled to the reference value for 1 MeV neutrons using the resistance factor *k*. This way, respecting to displacement damage, the fluence of impinging particles Φ can be replaced by an equivalent fluence of neutrons of 1MeV, $\Phi_{eq} = k\Phi$. A more detailed discussion is found in Refs. [18][19]

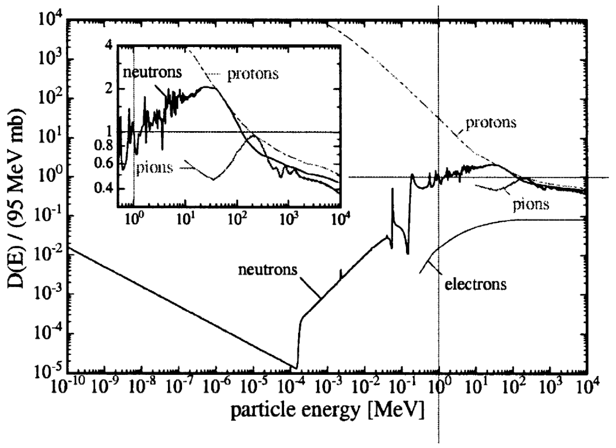

Figure 2.3: *Energy dependence of non-ionizing energy loss (NIEL) in silicon for various types of radiation.[19]*

The three main macroscopic effects [11] on high resistivity silicon detectors following energetic hadron irradiation are:

- Change of the effective doping concentration N_{eff} with severe consequences for the operating voltage needed for total depletion (higher depletion voltage).

- Fluence proportional increase in the reverse current, caused by the creation of generation-recombination centers.

- Deterioration of charge collection efficiency (CCE) due to charge carrier trapping leading to a reduction of the effective drift length both for electrons and holes.

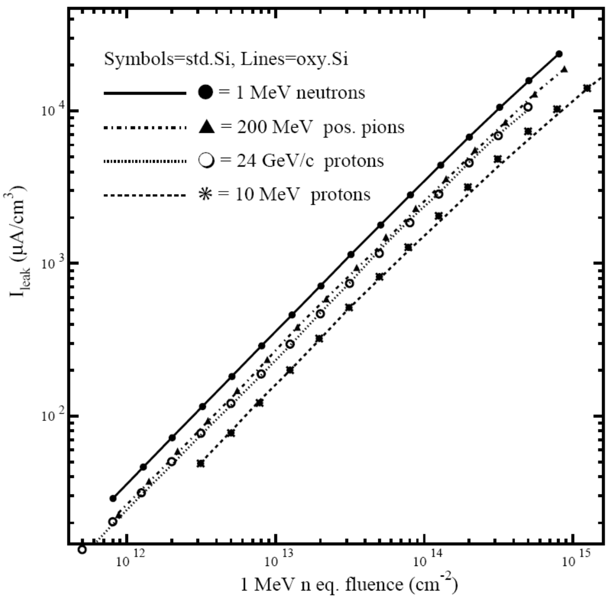

Figure 2.4: *Leakage current as a function of fluence for various irradiation types. Fluences are scaled with respect to 95 MeV·mb using the simulated values of NIEL [14].*

- **Surface damage due to Ionizing Energy Loss (IEL)**

Radiation damage on the surface of the detectors differs from bulk given the fact that bulk has a crystal structure and the surface region is composed by oxide (SiO_2) and the interface silicon-oxide, which are highly irregular, so the additional damage to the material structure caused by the interaction of radiation with the nuclei can therefore be safely ignored. Instead, it is the supply of charge carriers (electron-hole pairs) created by ionizing radiation what is important.

Table 2.1: *Values of some parameters for silicon and SiO_2 at 300K [20].*

Parameter	Si	SiO_2
E_g (eV)	1.124	8 – 9
μ_e (cm^2/Vs)	1417	20
μ_h (cm^2/Vs)	471	$\sim 10^{-8}$

The oxide regions can be modeled as high density volumes of charge states that can be changed by electrons or holes captures. Because of the high value of the energy gap of the oxide, see table 2.1, it is almost impossible that electrons (holes) generated in deep levels by irradiation could reach the conduction (valence) band and, as result, trapped charges in he oxides are obtained.

Most of trapped charge in the oxide is positive. It is because of the difference between electron and hole mobilities, which make the holes stay a longer time in the oxide and consequently our charge states will usually capture holes turning positive themselves. These semi-permanent trapped holes are located mainly in the Si/SiO_2 interface, in which high density of defects is higher, and increase the positive fixed charge in oxide, producing a shift in the flat-band voltage.

The positive charge in the oxide reaches a saturation value, it is explained by the number of semi-permanent traps in the oxide which is limited, and if all of them are filled, no further increase of the charge is possible. The value of $Q_{ox,sat}$ depends on the type or particle, energy, total absorbed dose, electric field during irradiation and the oxide properties, and usualy is 2-3 · 10^{12} cm^{-3} [21].

This charge accumulation in the oxide and the Si/SiO_2 interface affects the interstrip capacitance, introducing a noise factor, and in n-p and n-in-n strips detectors this positive charge produces an accumulation of electron from bulk forming an inversion layer, which leads to a decrease of the interstrip resistance and may short-circuit the strips.

Another factor to take into account is the annealing. Temporal measurements of irradiated silicon reveal that degradation in oxide is not stable and it is possible to get back to the initial state. That means that charge distribution in oxide depends on time through the time dependence of electric field, which is in last instance who rules charge movement. This process also depends strongly on temperature, allowing the process be carried out from milliseconds to years [21].

2.1.2 Bulk type inversion

In the previous section it was told that one of the NIEL effects is the change of the effective doping concentration, which leads to changes in the operating voltage to get full depleted. These changes represent the limiting factor for long-term detector operation. It is found that n-type detectors become progressively less n-type with increasing hadron fluence until they invert to effectively p-type at around 10^{13} $n \cdot cm^{-2}$, and then continue to became more p-type beyond this point, apparently without limit. The fluence at which this occurs is referred to as the *inversion fluence*. Typical results are shown in figure 2.5. In practice, the detectors still work beyond the inversion fluence because the junction moves from the p^+ strips to the n^+ back plane contact, leading to high electric field being located on the non-segmented side of the device. The depletion voltage required to operate a silicon detector is directly proportional to N_{eff} (see equation 04), hence at high fluences N_{eff} can be such that the required voltage exceeds the breakdown voltage on the device and efficient operation is no longer possible [22].

$$V_{FD} = \frac{q_e \omega^2}{2\varepsilon_{Si}} N_{eff} \tag{4}$$

This behavior is thought to be produced by deep acceptor levels which causes n-type silicon to become effectively p-type under bias, if are not biased they are intrinsic after heavy irradiation. First semiconductor simulations which include a single acceptor in the Poisson equation has been successfully used to describe the observed evolution of N_{eff} with fluence for both n-type and p-type detector material [23].

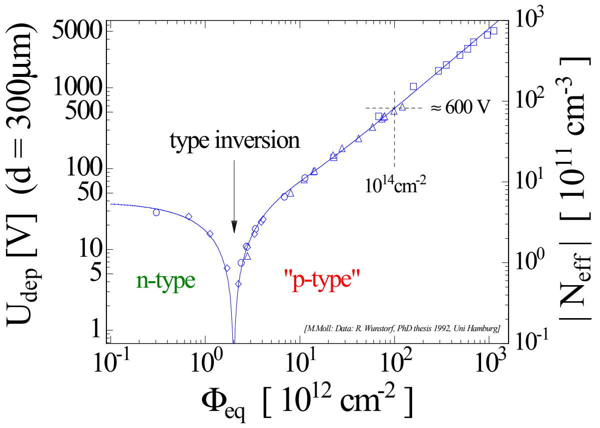

Figure 2.5: *Fluence dependence of the magnitude for the effective doping and full depletion voltage for a n-type silicon wafer irradiated with 1 MeV neutrons equivalent [15].*

2.1.3 Oxygen rich silicon

The primary defects in bulk due to radiation damage are interstitials (I), vacancies (V) and di-vacancies (V_2). These defects are not fixed, (I) and (V) are mobile at room temperature, while di-vacancies are static until 600K [24], and those who escape from recombination (I + V) diffuse through the crystal until they are trapped at impurity atoms or other defects. Table 2.2 shows the possible quasi-chemical reactions that can take place. The reaction rates depend on the concentration of impurities and defects and their relative capture radii.

Table 2.2: *Values of reactions and probabilities taken from references [25][26][27][28], where* $C_s + C_i \rightarrow CC$.

V reactions	Probability	I reactions	Probability
$V + I \rightarrow Si$	0.956	$I + I \rightarrow I_2$	0.118
$V + V \rightarrow V_2$	0.107	$I + V_2 \rightarrow V$	0.934
$V + V_2 \rightarrow V_3$	0.226	$I + V_3 \rightarrow V_2$	0.445
$V + O \rightarrow VO$	0.029	$I + VO \rightarrow O$	0.149
$V + VO \rightarrow V_2O$	0.139	$I + V_2O \rightarrow VO$	0.031
$V + V_2O \rightarrow V_3O$	0.043	$I + V_3O \rightarrow V_2O$	0.374
$V + P \rightarrow VP$	0.429	$I + VP \rightarrow P$	0.093
$V + I_2 \rightarrow I$	0.849	$I + C_s \rightarrow C_i$	0.093
$V + ICC \rightarrow CC$	0.149	$I + CC \rightarrow ICC$	0.673
$V \rightarrow ICC \rightarrow CO$	0.298	$I + CO \rightarrow ICO$	0.336

P, O and C are phosphorous, oxygen and carbon respectively. P is the donor material for the n-type bulk, O and C are impurities of crystal during its formation. C is divided in C_i and C_s, given the fact that both C and Si belong to group IV and, in addition to C_i interstitial, we can find carbon substitutional C_s, that are what matter because of the low migration velocity of the carbon interstitial at room temperature [29].

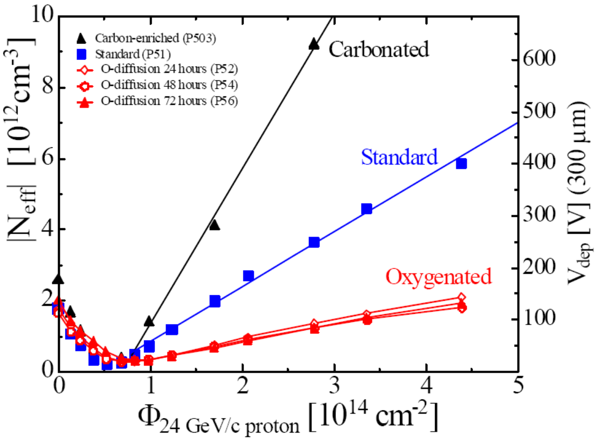

Figure 2.6: *Influence of carbon and oxygen enrichment to changes of the effective doping concentration after proton irradiation [15].*

The VO defect itself has no significant influence on the electrical properties of the silicon. However, evolution of VO formation as a function of fluence (figure 2.7 a) has an important paper in the formation of V$_2$O defect, which has been proposed as a possible candidate of deep acceptor state to explain changes of Neff. Oxygen enrichment of silicon (figure 2.6) is used to prevent fromV$_2$O formation [22], this is because the oxygen getters the vacancies produced during irradiation and suppresses the channel V + VO → V$_2$O. But it seems to be not true at all. NIEL and formation defects simulations reveal that a high concentration O is suppressing V$_2$O production only at fluences well beyond 10^{13} cm^{-2}. At low fluencies an increase of oxygen leads to a higher V$_2$O production. The exception is neutron irradiation, where V$_2$O production within the cluster appears to dominate at all fluences, independent of oxygen concentration [14]. Curves of this behavior are shown in figure 2.7 b.

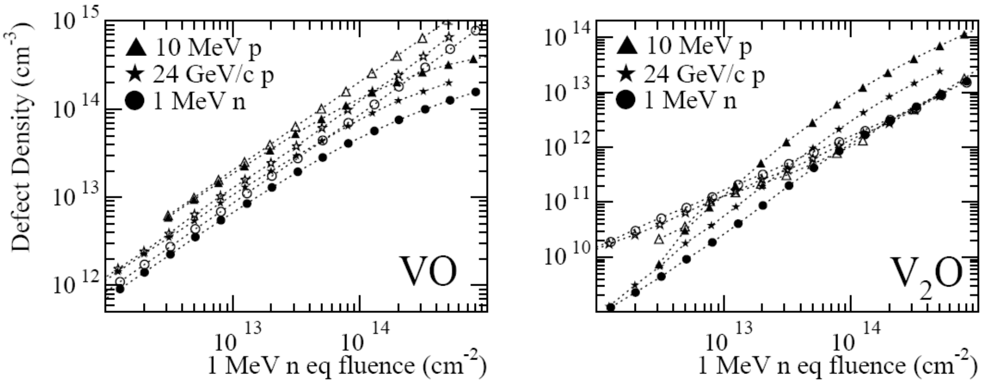

Figure 2.7: *Concentration of VO (left) and V$_2$O (right) defects as a function of hadron fluence. Solid symbols correspond to silicon with an initial oxygen concentration of $5{\cdot}10^{15}$ cm^{-3} , open symbols to $5{\cdot}10^{17}$ cm^{-3}[14].*

- **Different silicon materials**

Different types of silicon wafers have been used for the fabrication of silicon detectors. Float Zone (FZ) silicon shows best results due to its uniformity, but FZ n-type silicon wafers present space charge sign inversion (SCSI), so the use of oxygenated materials is needed. Diffusion Oxygenated Float Zone (DOFZ), Czochralski (CZ) and Magnetic Czochralski (MCZ) silicon are materials which contain a variable amount of oxygen concentration. CZ and MCZ silicon materials are produced in quartz crucibles and contain, due to the solution of quartz (SiO_2) crucible into the silicon melt, an even higher oxygen concentration ranging from 4 to $10 \cdot 10^{17}$ cm^{-3} depending on the specific CZ or MCZ growth technique, while 1 - $3 \cdot 10^{17}$ cm^{-3} is the range for DOFZ material. Only recently CZ and MCZ silicon became available with a high resistivity to be used as detector material.

In the framework of RD50 project Czochralski (CZ) silicon from Sumitomo-Sitix, Japan (600 Ocm, n-type, <100>, [O] = $8 \cdot 10^{17}$ cm^{-3}) and Magnetic Czochralski (MCZ) from Okmetic Ltd, Finland (900 Ocm n-type and 2 kOcm p-type, <100>, [O] = $5 \cdot 10^{17}$ cm^{-3}), have been investigated. Experiments were carried out using high energy (23 GeV [30]) and low energy (10, 20, 30 MeV [31]) protons, 190 MeV pions [30], 900 MeV electrons [32] and ^{60}Co γ-rays [16moll] revealing clear advantages of MCZ and especially CZ silicon against FZ and DOFZ silicon.

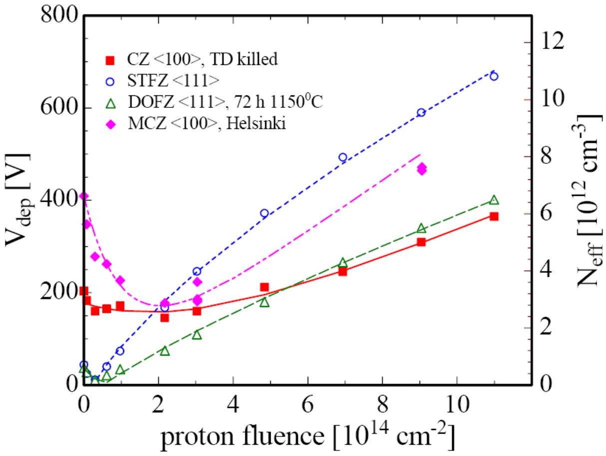

Figure 2.8: *Comparison of standard (FZ) and Oxygenated (DOFZ) Float Zone silicon with Czochralski (CZ) and Magnetic Czochralski (MCZ)silicon pad detectors with 23 GeV protons at CERN [30]*

In figure 2.8 we can see an example of an irradiation experiment performed with 23 GeV protons. At first sight we see lower depletion voltages for CZ materials than FZ for high fluences, but in more subtle experiments using Transient Charge Technique (TCT) it has found that CZ and MCZ do not undergo type inversion up to the highest fluence investigated here while the effective trapping times are very similar to the ones of FZ and DOFZ silicon [30] (in contrast with neutron irradiation in which FZ, DOFZ, CZ and MCZ present all SCSI, although this latter only under high dose [11]). These results are confirmed by recent results in MCZ and EPI-Si detectors, and besides reveal that V_{fd} and by that $|N_{eff}|$ always increase after applying the bias regardless on space charge sign. In n-type material that doesn't undergo SCSI the effective donors are activated and the high electric field will stay on the segmented side of the device even after high fluences [34].

Those oxygen related thermal donors, which appear in oxygen-rich Si when annealed in the temperature range 300-550 ºC, may be the responsible of the absolute effective doping concentration increase with fluence. In standard FZ silicon they are formed only in negligible concentration due to the low oxygen content. Therefore, negatively charged radiation induced defects dominate. In DOFZ silicon some donors are formed compensating a part of the negatively charged defects leading to a reduced depletion voltage after type inversion. In CZ silicon the radiation induced donors overcompensate the negatively charged defects leading to a net increase of the absolute effective doping concentration, this time with a positive space charge.

Potential threat of thermal donors forming during processing of CZ, MCZ and DOFZ detectors and leading to a lower resistivity can be overcome by a thermal donor killing processes applied to the devices after processing. The formation of thermal donors offers however also the possibility to tailor the starting resistivity to a specific value [35].

2.1.4 Annealing effects

Induced defects in silicon are not stable but they present annealing effects that affect to leakage current, effective trapping times and space charge density.

Annealing consists of exposition to middle and high temperatures to induce the removal of radiation defects by recombination of vacancies and interstitials. Effective doping concentration after irradiation can be described by three terms according to *Hamburg model* [35]: the decay of effective acceptors immediately after irradiation (*beneficial annealing*), stable part (*plateau*) and creation of the effective acceptors at late annealing stages (*reverse annealing*). Graphs of this behavior are shown in figure 2.9.

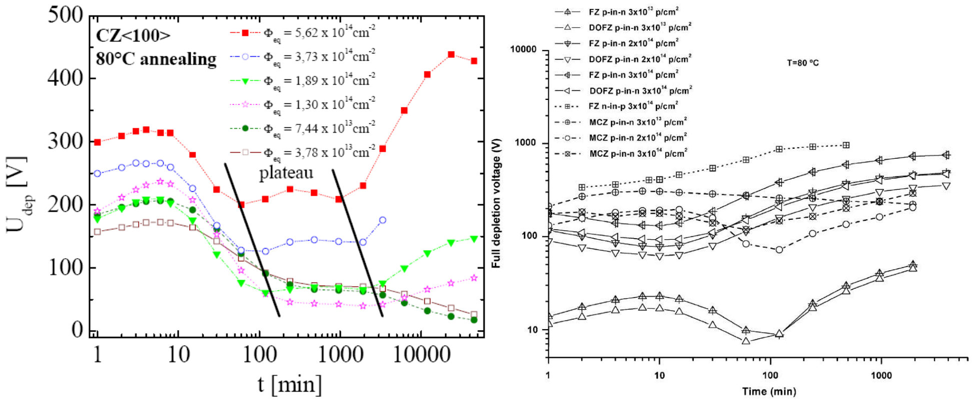

Figure 2.9: *Evolution of full depletion voltage with time, under 80 ºC annealing of high resistivity CZ silicon (left) [30], MCZ, FZ and DOFZ silicon irradiated with 24 GeV protons [36].*

Leakage current constant α(t), which is confirmed to be independent on material and irradiation particles [11], is also affected by annealing.

$$\alpha = \frac{\Delta I}{V \cdot \phi_{eq}} \tag{5}$$

where ΔI is the change in leakage current after irradiation, V the detector volume and Φ_{eq} is the neutron equivalent fluence.

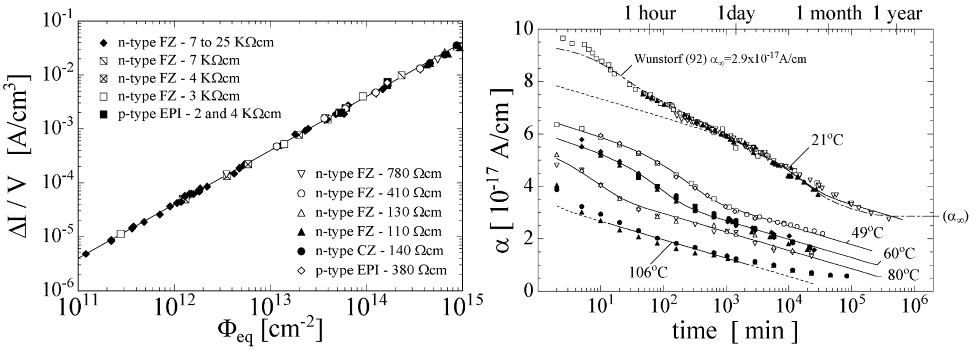

Figure 2.10: *Material independence of current related damage α (lefit) and also as function of accumulated annealing time at different temperatures [35].*

2.1.5 P-type detectors

The type inversion of p-in-n detector is posing a problem since the high electric field is switching from the structured readout side to the back side of the detector accompanied by a loss in spacial resolution and, if not operated with voltages well above the depletion voltage, by reduced charge collection efficiency (CCE). This is the reason why the more expensive n-in-n technology is used for pixel detectors in harsh radiation environments. After type inversion the high electric field will be placed on the structured side of the device and so the holes have to move crossing an undepleted region with low electric field (figure 2.11), decreasing the charge collection efficiency. Hence it is a promising approach to investigate n-in-p detectors which do not type invert (they are already p-type) and for which the structured readout side will be the one with the high electric field before and after irradiation [11].

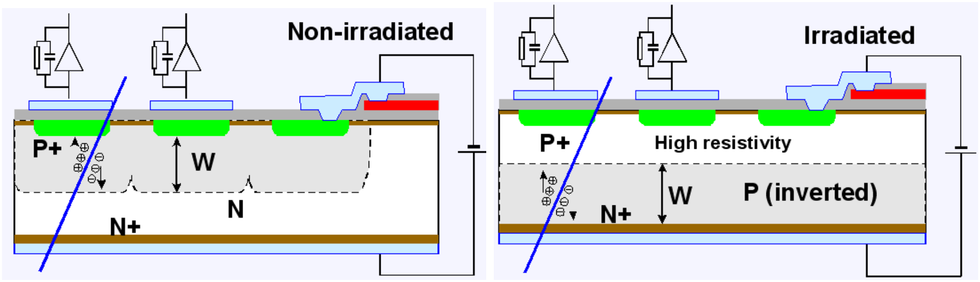

Figure 2.11: *Cross section of biased n-type detectors before (left) and after (right) irradiation.*

Microstrip detectors on p-type silicon present the challenge of achieving a proper interstrip insulation. At the silicon/oxide interface, positive charges are always present and will increase when the detectors are irradiated. This will cause electrons from the bulk silicon to accumulate at the silicon surface forming an inversion layer, which leads to a decrease of the interstrip resistance and may short-circuit the strips.

Different solutions for the insulation of strips are the following [12]:

- *p-stop*, which consists on a p-type ring surrounding n-type strips. These p-stop rings interrupt the electronic inversion layer and provide a complete isolation, but has the inconvenient of an extra photolithographic step compared to standard p-n detectors, increasing costs. Besides microdischarges appear in the leakage current and in the electronic noise, which are produced in intense electric fields, as occurs in the edges of p-stops when a sufficiently high potential difference is applied.

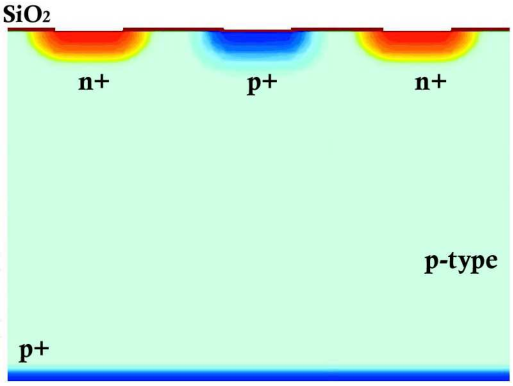

Figure 2.12: *P-stop method for the insulation for n-type strips.*

- *p-spray*, it is simpler than p-stop and consists of an uniform p-type implantation on the whole wafer before the fabrication steps, balancing the electronic inversion layer. Various studies have demonstrated that irradiated detectors treated with p-spray present better behavior than p-stop detectors [37][38][39]. However, for having a correct insulation and prevent from a low breakdown voltage the implantation profile needs to be calibrated carefully.

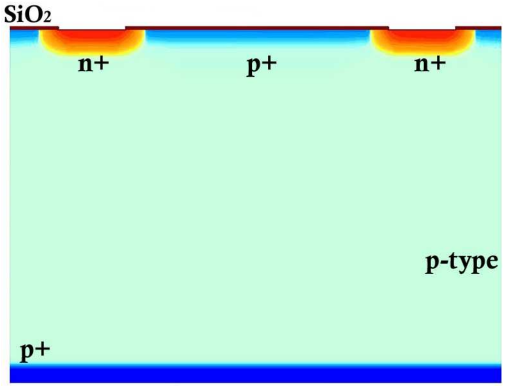

Figure 2.13: *P-spray method for the insulation for n-type strips.*

- *moderated p-spray*, it is a combination of a p-stop insulation and a light p-spray. P-stop insulation guarantees the insulation of strips while p-spray, which prevents from microdischarges, consists of a thin layer for prevent from having a low breakdown voltage [40].

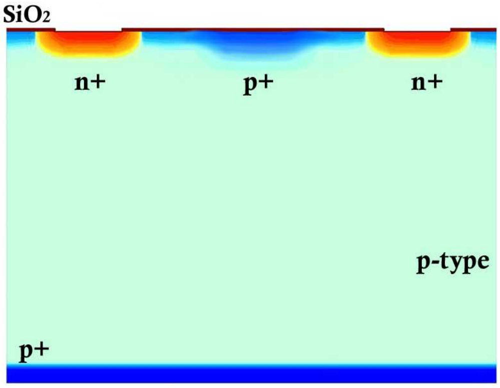

Figure 2.14: *Moderated p-spray method for the insulation for n-type strips.*

Irradiation studies [41][42] gave evidence of a sensitive improvement in the CCE performances of detectors fabricated in p-type material (with n side read out).

2.2 Measurements

The results of the measurements of the microstrip detectors fabricated at CNM for the RD50 collaboration will be exposed in this section. These data were taken before (at CERN characterization laboratory, Geneve) and after (at IFIC characterization laboratory, Valencia) irradiation. Previously I will describe the setup installations were these measures were carried out.

2.2.1 Setup at CERN

At CERN we had at our disposal one complete equipment (figure 2.15) to measure the characteristics IV and CV of microstrip detectors with very low levels of noise. The room temperature is also controlled by an air conditioning device which is working continually.

Figure 2.15: *Computer used for monitoring the measurements and for data collection (left). Keithley485, Keithley 2410, Agilent 4263B, Keithley 237 and IV-CV coupling box (right).*

A probe station is used for the electrical characterization of microstrips detectors. The probe is located inside a Faraday box connected to ground for a good insulation from outer electromagnetic signals that can increase the noise levels. This Faraday box also avoids the entry of light that interact with the radiation detector increasing the leakage current by releasing charge carriers. The probe station (figure 2.16) is placed at 1 meter above the floor supported by 4 height-variable steel beams for movement insulation.

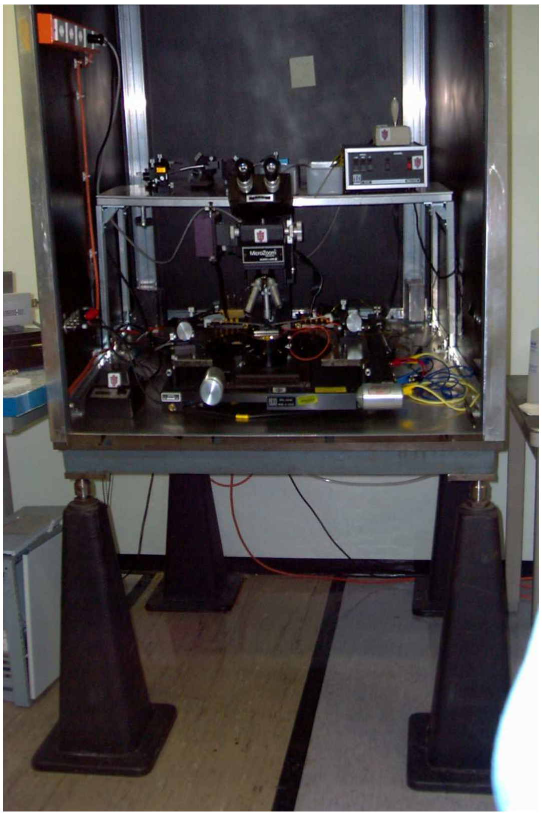

Figure 2.16: *Picture of the probe station inside the Faraday box.*

For the IV characteristics we used a Keithley 485 for measuring the leakage current while a Keithley 2410 is used for biasing the backplane. Guard ring is connected to ground in both IV and CV characteristics. For CV we used a Keithley 485 for measuring the leakage current, a Keithley 237 for biasing the backplane and an Agilent 4263B for measuring the capacitance of the detectors.

2.2.2 Setup at IFIC

Once the detectors have been characterized they have to be irradiated at different neutron fluences. After irradiation, electrical characterizations were carried out at IFIC (Instituto de Física Corpuscular, Valencia, Spain) facilities. IFIC has equipments for laser and beta measurements for charge collection efficiency of the detectors. Beta measurements are needed to obtain the maximum charge collected by particle in the silicon detector to calibrate the results obtained using the laser beam.

During the measurements the detectors are fixed on a PCB to measure the electrical parameters while are illuminated with beta or laser sources, and placed in a metal box that provides the electrical connectors. This box is placed inside a Faraday box for electromagnetic insulation (figure 2.17a), saturated with nitrogen to maintain a dry environment. The Faraday box is located inside a freezer at -30ºC to reduce leakage current.

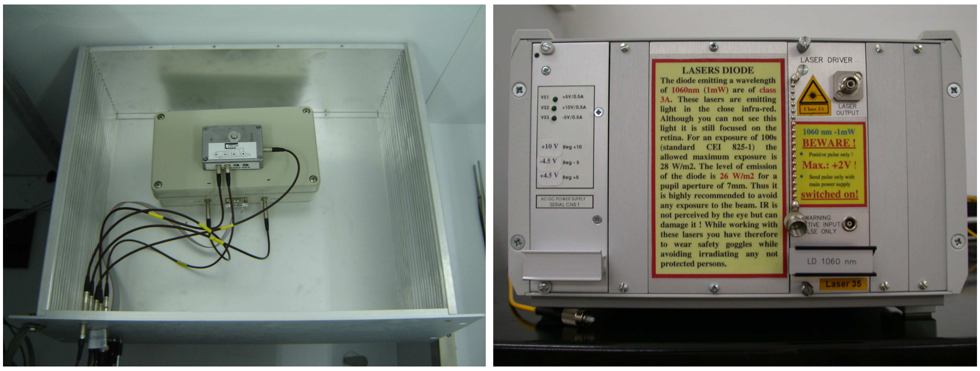

Figure 2.17: *Pictures of the metal box (left) and the laser source (right).*

Beta irradiation is carried out by using a ^{90}Sr source, with an energy deposition comparable to minimum ionizing particles (mip), whose activity is 10 kBq (date: 1 June 2006), for laser irradiation a laser beam of 1mW is used, corresponding to class 3A (figure 2.17b). The use of this laser beam and a pulse generator provide laser pulses that are driven to the Faraday cage through optic fibers. Details of both beta and laser sources are shown in table 2.3.

Table 2.3: *Parameters of laser (left) and beta (right) sources.*

Laser source	
Wavelength	1060 nm
Energy	1.17 eV
Power	1 mW

Beta source	
Half-life	28.9 y
Energy	0.546 MeV
Product	^{90}Y

Finally, the signals from both mip and laser are read through an oscilloscope and are saved for their later analysis using ROOT software [43].

2.2.3 Results

In the first stage we got IV characteristics of all the detectors, and CV only for some of them for getting an approximate estimation of the full depletion voltage of each type of wafer. Those values give us information about the functioning of the detectors to select the ones with better behavior to do the neutron and proton irradiations. Collected data are shown in table 2.4.

Table 2.4: *Values of some of the most relevant parameters of microstrip detectors fabricated at CNM-IMB for the RD50 collaboration.*

Wafer	Growing Method	Type	Thickness (µm)	Nominal Resistivity (Ω·cm)	Wafer Origin	Average V_{FD} (V)	Measured detectors	Calculated Resistivity[1] (Ω·cm)	Average I at V_{FD} (per cm^{-2})	Selected detectors
1	FZ	n-p	300 ± 15	30k	CNM	42	2	22k	35 nA	14 (23)
4	FZ	n-p	300 ± 15	30k	CNM	37	2	25k	175 nA	18 (26)
5	DOFZ	n-p	300 ± 15	30k	CNM	40	3	23k	285 nA	19 (25)
6	DOFZ	n-p	300 ± 15	30k	CNM	37	2	25k	265 nA	19 (26)
7	DOFZ	n-p	300 ± 15	30k	CNM	52	1	18k	874 nA	21 (26)
8	DOFZ	n-p	300 ± 15	30k	CNM	40	25	23k	136 nA	21 (26)
9	DOFZ	n-p	300 ± 15	30k	CNM	39	2	24k	165 nA	20 (23)
10	MCZ	n-p	300	> 2k	RD50				863 nA	21 (25)
11	MCZ	n-p	300	> 2k	RD50				1.0 µA	16 (25)
12	MCZ	n-p	300	> 2k	RD50	238	2	3.9k	8.4 µA	21 (26)
13	MCZ	n-p	300	> 2k	RD50				328 µA	9 (12)
14	MCZ	n-p	300 ± 25	1k	CNM				> 1 mA	22 (22)
15	EPI	n-p	~ 150		RD50	225	2	4.1k	16 µA	21 (24)
16[2]	EPI	n-p	~ 150		RD50					
17	FZ	n-in-n			CNM	39	2	24k	70 µA	22 (26)
18	FZ	n-in-n			CNM	42	1	22k	91 µA	22 (26)
19	MCZ	p-n	300 ± 25	> 500	RD50				5.8 nA	21 (25)
20	MCZ	p-n	300 ± 25	> 500	RD50				5.0 nA	22 (26)
21	MCZ	p-n	300 ± 25	> 500	RD50				7.1 nA	19 (26)
22	MCZ	p-n	300 ± 25	> 500	RD50				3.7 nA	22 (26)
23	EPI	p-n	~ 150		RD50	181	2	5.1k	5.0 nA	13 (17)

---

[1] Wafer 16 was not measured

[2] Using Thurber's equation

These values for leakage current are taken at V_{FD} + 50-100 V. This is done in order to homogenize the measurements since substrate with different resistivities have different full depletion voltage values. In the calculus of the averaged leakage current only the detectors which have a $V_{Break} > V_{FD}$ were used. There are two numbers in the last column, 14 (23) i.e., the first number means the quantity of detectors used in the calculus of the average leakage current, and the second one, inside parenthesis, shows the amount of available detectors. The rejected data were those whose value was above 2.5 times the sample standard deviation.

Mean values of leakage currents and full depletion voltages for the different types of wafers are shown in figures 2.18 and 2.19 respectively. In this table we can appreciate the differences between wafers: float zone have 40V for depletion voltages while Czochralski and epitaxial reach depletion voltages higher than 200 V. The nominal resistivity of the wafers is 30 kΩ·cm for float zone and more than 2 kΩ·cm in the case of Czochralski. There are no known values for the nominal resistivity of the epitaxial wafers.

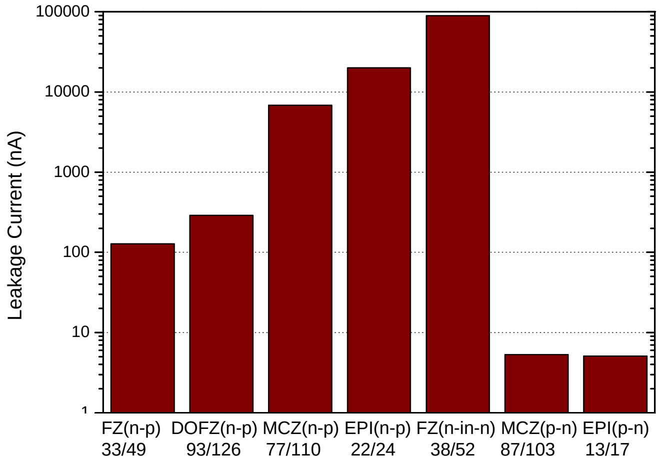

Figure 2.18: *Bar diagrams of mean leakage current values for each type of wafer.*

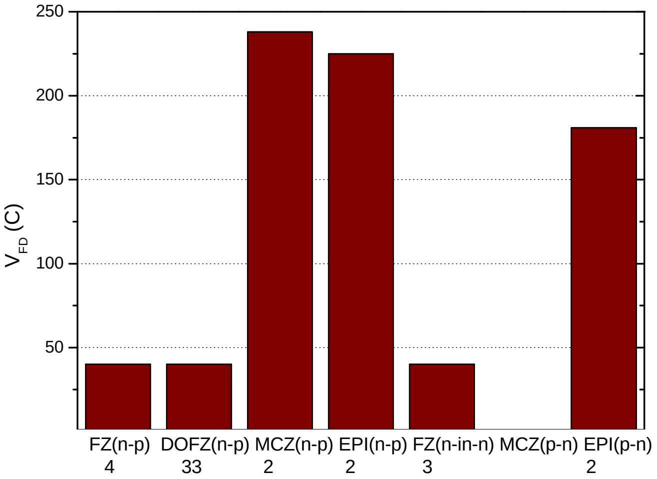

Figure 2.19: *Bar diagrams of averaged full depletion voltage for each type of wafer.*

All of the microstrips detectors of one of the wafers (DOFZ 08) were electrically characterized (curves I-V and C-V) for an analysis of their distribution on the wafer. In figures 2.20 and 2.21 are shown the wafer maps of full depletion voltages and leakage current (at full depletion voltage), It can be noticed that full depletion voltage values are all around the value 40V, that corresponds to $N_{eff} = 5.7 \cdot 10^{11}$ cm^{-3} and 23.3 kΩ·cm, using equation (4) and Thurber's polynomial respectively. The leakage current in those microstrip detectors, in general, has values sufficiently low for their use in the experiments. Only one of these wafers presents wrong behavior, wafer 14, possibly because of the fabrication process.

$$N_{eff} = \frac{N_D N_A}{N_D + N_A} \tag{6}$$

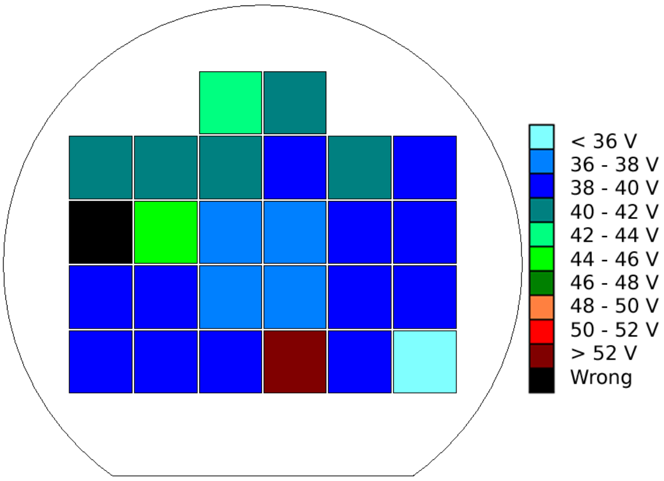

Figure 2.20: *Wafermapping of full depletion voltage for wafer RD50-08 DOFZ-p, fabricated at CNM-IMB.*

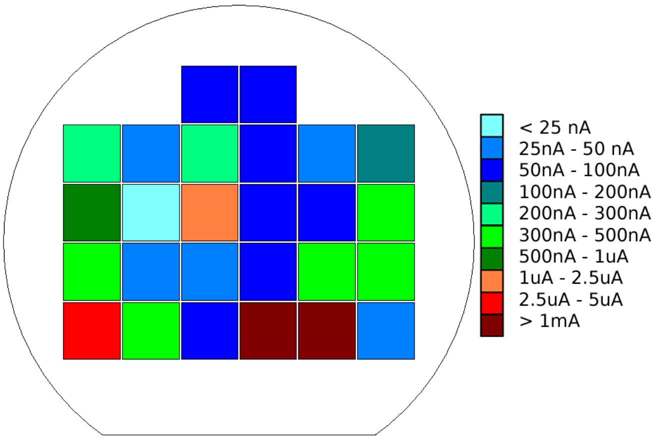

Figure 2.21: *Wafermapping of leakage current at full depletion voltage+100V for wafer RD50-08 DOFZ-p, fabricated at CNM-IMB.*

After the electrical characterization of all RD50 strips detectors, the next step consisted on the irradiation and following measurements of some of these detectors. The detectors were irradiated with neutrons at different fluences, from 10^{14} n/cm^2 to 10^{16} n/cm^2, in the nuclear reactor for investigation TRIGA MARK II of the Josef Stefan Institute in Ljubljana, Slovenia. First results of these irradiations can be found in [42][44] for FZ detectors.

Results of DOFZ detectors irradiated with neutrons are shown in figure 2.22. For the unirradiated sample, the plateau corresponding to full depletion is reached near 50 V. For the samples irradiated at high fluences, the plateau is not reached up to 900 V, although the curve corresponding to the fluence $3 \cdot 10^{14}$ n/cm^2 undergoes a change in the slope near 500 V.

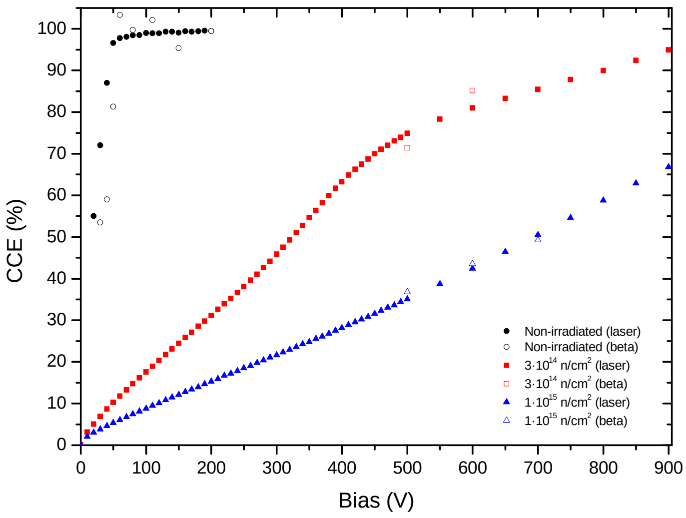

Figure 2.22: *Graph of charge collection efficiency (CCE) vs the bias. Wafer 5 corresponding to DOFZ p-type.*

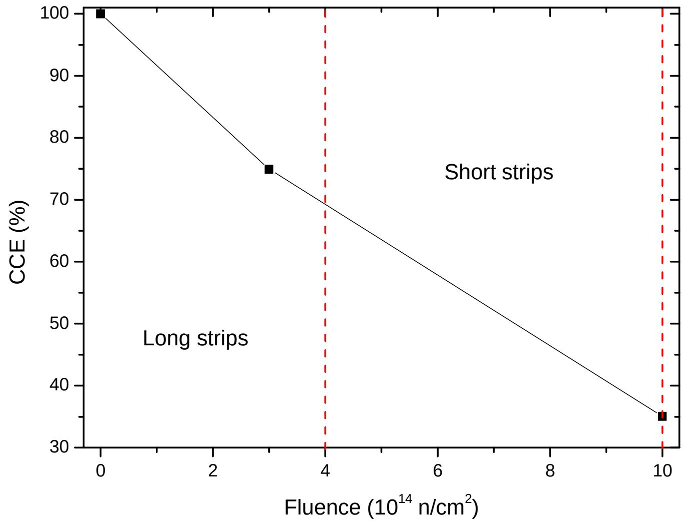

Figure 2.23: *CCE as a function of the fluence for a 500 V bias. Wafer 5 (DOFZ p-type).*

Figure 2.23 shows the charge collection efficiency at a fixed bias set to 500 V for the three measured samples from the figure 2.22. The efficiencies present a decreasing behavior as the fluence increases, as expected due to the cumulated radiation damage.

2.3 Conclusions

Microstrip detectors of different types of doping and fabrication process wafers were measured. About p-type substrate wafers, FZ and DOFZ were the ones with the lowest leakage current (~ 200 nA) and full depletiom voltages (~ 40V). MCZ and EPI reached values of leakage current higher (~ 10 µA) and their full depletion voltages were the highest of all the measured wafers (above 200 V). Those values of V_{FD} are related with the resistivity of the wafer and, as can be seen in table 2.4, they are similar to the nominal values.

Concerning the n-type wafers, the FZ(n-in-n) microstips detectors had values in the same range that p-type FZ (~ 40 V) but the leakage currents reached values nearly to 0.1 mA, very high taken into account they were taken at 100 V. The V_{FD} of the EPI microstrip detectors were about 180 V, 20% less than for EPI p-type. There is no information about the V_{FD} of the MCZ microstrips detectors because of break voltages (V_B) were about 400 V and the V_{FD} were not reached at those voltages. From previous collected data on PAD detectors, the V_{FD} measured were above 1000 V. The reported leakage currents in table 2.4 were measured at 300 V. Measured leakage currents of MCZ and EPI were quite low ~ 5 nA.

ATLAS SCT Specifications [45] for silicon microstrip detectors demand p-type Floatzone wafers with a thickness of 320 ± 15 µm. These conditions only allow the use of wafers 1 to 9, which satisfy too the electronical conditions: initial depletion voltage < 500 V, wafer resistivity is to be > 4 kΩ·cm and initial leakage current, normalized to 20ºC, < 200 µA at 600 V (or the onset of microdischarges).

The wafer mapping, see figures 2.20 and 2.21, shows that, in general, the lowest values for full depletion voltages and leakages currents are in the center of the wafer, and grow as are closer to the edge.

The measurements of the charge collection efficiencies after irradiadion at $3\cdot10^{14}$ and $1\cdot10^{15}$ n/cm^2 show that they are still been operational for the use under those doses.

The realization of this work was very useful for me to learn the use of the equipments for the electrical characterization of the irradiated and unirradiated detectors. Besides, to learn the way in which irradiated detectors are treated to avoid their annealing, and their study of charge collection efficiency by using beta and laser sources.

3 Simulation of irradiated edgeless detectors

In this chapter simulation results of irradiated edgeless detectors for the TOSTER collaboration are presented. For this purpose, the detector response of particle tracking was simulated, introducing the defects caused by the diamond saw cut when dicing detectors from the wafer by a gradient of charge traps from the edge, and the radiation induced defects which were modeled in the bulk as traps in deep acceptor/donor levels and in the Si/SiO$_2$ interfaces as different space charge concentrations.

3.1 Introduction to ISE-TCAD (Sentaurus)

Technology Computer-Aided Design (TCAD) refers to the use of computer simulations to develop and optimize semiconductor processing technologies and devices. Synopsys TCAD software solves fundamental, physical partial differential equations, such as diffusion and transport equations, to model the structural properties and electrical behavior of semiconductor devices. This deep physical approach gives Synopsys TCAD simulation predictive accuracy for a broad range of technologies. It is therefore practical to use TCAD simulations to reduce the costly and time-consuming test wafer runs when developing and characterizing a new semiconductor device or technology.

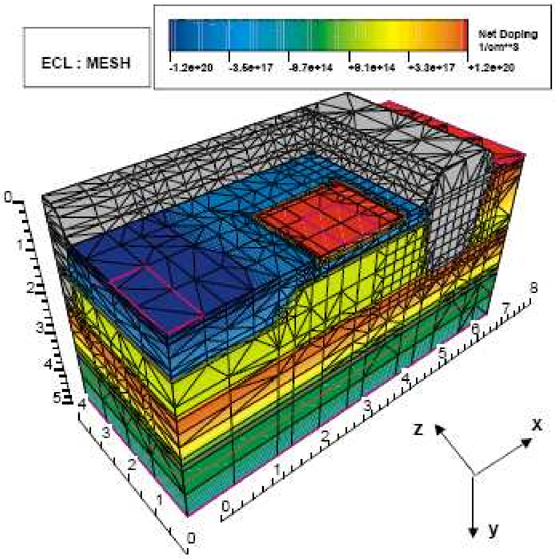

Figure 3.1: *ECL transistor created by MESH.*

For the studies I used some of the tools provided by Sentaurus (and ISE-TCAD, the previous version of this Software tools pack) [46]. These tools are listed below:

- DIOS, which is a multidimensional process simulator for semiconductor devices. It allows simulations of complete fabrication sequences including etching and deposition, ion implantation, and diffusion and oxidation with identical models in one dimension and two dimensions.
- MDRAW, which offers flexible 2D device boundary editing, and doping and refinement specifications. MDRAW communicates with the other ISE TCAD tools using the DF–ISE data format. The 2D meshing engines are integrated in MDRAW and are available without using file input and output.
- MESH, is a dimension-independent tool, which incorporates several different meshing[1] engines, using different meshing techniques and algorithms. MESH has been used in this work for meshing the 3D detectors, although it can be used too for 2D devices instead of MDRAW. Local mesh refinement is performed by using the doping and refinement information prescribed in the MESH command file.
- SENTAURUS DEVICE (SDEVICE), is an advanced 1D, 2D and 3D device simulator capable of simulating the electrical, thermal and optical characteristics of silicon and compound semiconductor devices.
- TECPLOT, is a plotting software with extensive 2D and 3D capabilities for visualizing data from simulations and experiments, such as electric field, holes current densities, doping levels, etc.
- INSPECT, is a curve display and analysis program. It works with curves specified at discrete points. Inspect enables users to work interactively with data using both a graphical user interface and a script language.

3.2 Edgeless detectors

TOSTER collaboration has the aim of extend the use of edgeless detectors used in close to beam experiments to other applications. This is the case of the LHC TOTEM Experiment [5] that has placed silicon detectors in special beam insertions (Roman Pots) as close as possible to the beam, to track protons elastically scattered from the interaction point 5 of the LHC.

TOSTER collaboration will also investigate the radiation hardness properties of edgeless detectors for the future SLHC upgrade, in which will take place high radiation fluences.

Edgeless detectors developed by the LHC TOTEM collaboration are fully sensitive within 50 µm from their physical edges employing standard planar fabrication techniques and diamond saw dicing. Applications of

---

[1] Meshing is the process of making a mesh in which SDEVICE software will carry out its calculus in each vertex.

edgeless detectors range from synchrotron imaging to high energy physics experiments.

The TOTEM experiment requires two different types of silicon detectors for detecting leading protons in the Roman Pots [47][48]. Both technologies respond to the crucial requirement of a very small insensitive volume at their physical edges to be fully efficient at 1 mm from the beam. These edgeless silicon detectors are respectively called Planar Edgeless Detectors with Current Terminating Structure (CTS) [49] and 3D/Planar Edgeless Detectors with Active Edges [50].

In the Planar Edgeless Detector the CTS occupies the first 50 μm from the cut edge, after which the sensitive volume starts. In this case, the voltage applied to bias the device has to be applied also across the die cut via an implanted ring that runs along its physical edge. This external ring, called the current terminating ring, collects all the surface current from the cut avoiding its diffusion into the sensitive volume. A schema of the CTS is shown in Fig.3.2.

3.2.1 Edge design (CTS)

Due to the high concentration of defects that takes place in the edge because of the diamond saw cut, a high conductivity is produced in the cut surface that generates a screening of the electrical field in the adjacent regions. Besides we must to add that under an oxidizing atmosphere it is produced the oxidation of the outer layer of silicon, giving place to the formation of an oxide layer, SiO_2. This oxide layer reduces the conductivity of the cut surface. Combining both behaviors it is not possible to have well determined the properties of the edge.

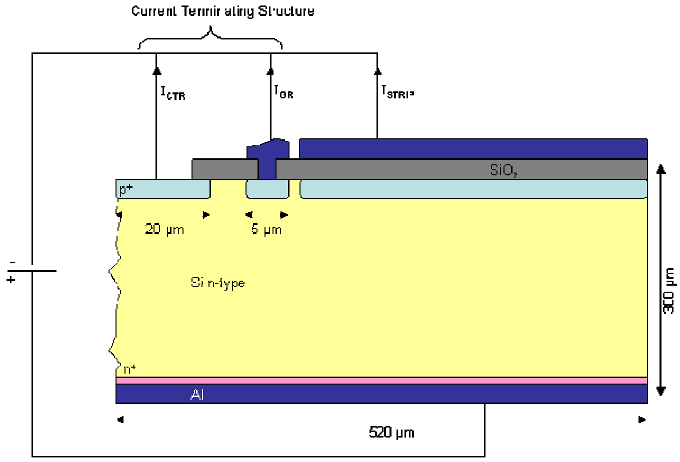

Figure 3.2: *Cross-section of an edgeless silicon detector which has been cut using a diamond saw. The drawing is not to scale.*

To solve this problem terminating structures are modeled. The basic idea is to apply the full detector bias across the detector chip cut (Current Terminating Ring) and collect the resulting leakage current on an outer ring (Guard Ring), which surrounds the active area and which is biased at the same potential as the detection strips. This ring is separated from the detector biasing electrode (the strips are biased by means of a punchthrough structure between this biasing electrode and the strips). Separating and biasing these two rings at the same potential strongly reduces the influence of the current generated at the detector edge on the active detector volume. In contrast with other ring structures which provide voltage termination, this structure terminates the current and, therefore, it is called Current Terminating Structure" (CTS) [49].

3.2.2 Physics and parameters

At first place we simulated the behavior of the unirradiated edgeless detector. For this purpose we started the simulation process using DIOS software. This program allowed us to simulate all the steps that take place in a fabrication process, such as oxidation, etching, ion implantation, metallization, etc. Although the fabrication processes take place in both sides, simulation was only carried out on the top surface, taking into account all the processes, using a silicon layer of 50 µm for saving CPU time. The rest of the bulk and the bottom implantation were added by using MDRAW software. This program was used as well to build the mesh for the final simulated detector.

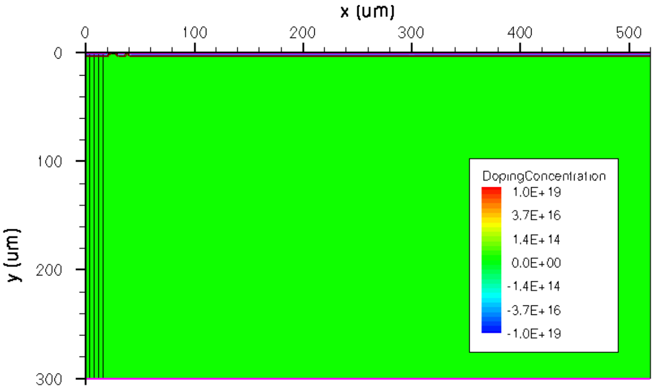

Figure 3.3: *View of the doping concentration in the whole detector.*

The size of the simulated detector is 520µm × 300µm, the concentration of Phosphorous in the bulk is $5{\cdot}10^{11}$ cm^{-3}, and Boron concentration at top is $5{\cdot}10^{17}$ cm^{-3} and at bottom is $1{\cdot}10^{20}$ cm^{-3}. The surface regions without implantation were covered with passivating oxide layers. The fixed charge which forms in real devices at the silicon-oxide interface is modeled by a positive uniform charge, which was set to $4{\cdot}10^{11}$cm^{-3} before irradiation and 10^{12}cm^{-3} after irradiation. In all simulations, the temperature was set to room temperature.

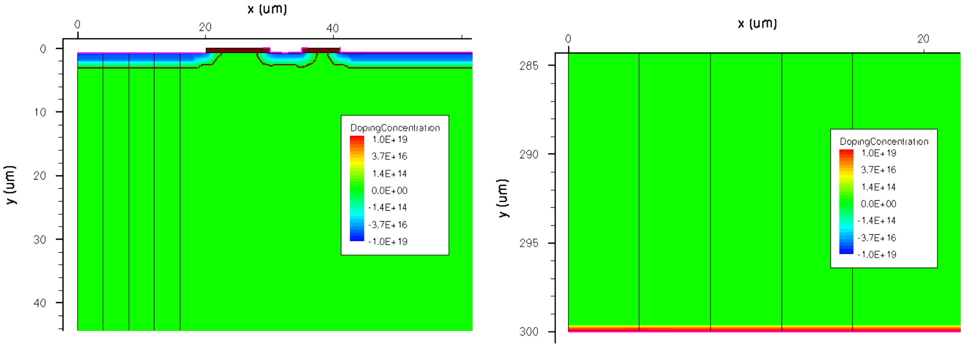

Figure 3.4: *Close look of doping concentration of top and bottom regions.*

3.2.2.1 Sawcut damage model

Next step consisted in the modeling of the detector edge. To model the rough and cracks of the surface and the outer region, due to the cut of the wafer using a diamond saw, we introduced charge traps. These traps were designed by using a gradient from the surface divided in four zones, due to the fact that ISE-TCAD software did not allow to implement a gradually decreasing concentration profile from the edge. It was necessary to create 4 different profiles taking into account the decreasing concentration of traps [49]. These four regions were designed by MDRAW software and parametrized in the command file of SDEVICE program.

Traps of each one of these 4 regions consist of 2 neutral electron (1, 2) and 2 neutral hole (3, 4) types with exponential distributions, given by the following function [46]

$$f_t(E) = N_1 e^{-\left|\frac{E-E_C}{E_{S1}}\right|} + N_2 e^{-\left|\frac{E-E_C}{E_{S2}}\right|} + N_3 e^{-\left|\frac{E-E_V}{E_{S3}}\right|} + N_4 e^{-\left|\frac{E-E_V}{E_{S4}}\right|} \qquad (7)$$

Where N_1 and N_2 give us the electron traps concentrations and in the other hand N_3 and N_4 give us the hole traps concentrations, E_{S1} and E_{S2} are the standard deviations for electron traps while E_{S3} and E_{S4} are standard deviation for hole traps. Fig 3.5 shows a graph of the distribution function of neutral electron and hole traps.

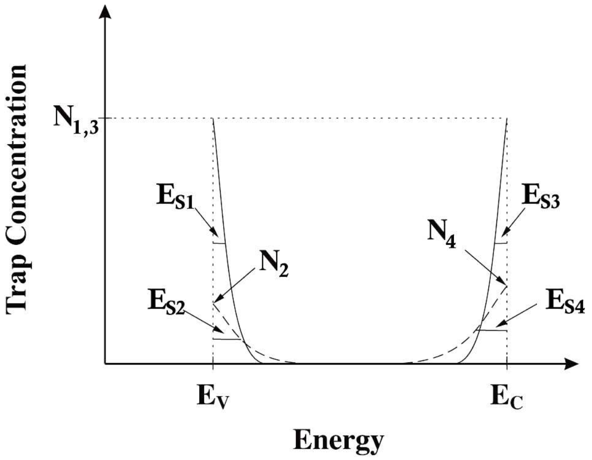

Figure 3.5. *Energy levels distribution in the forbidden gap for polysilicon with four exponential distributions [49].*

Constant values for traps concentration in the 4 zones follow the next equation

$$(N_{1,2,3,4})_m = (N_{1,2,3,4})_0 \times 10^{-m}, m = 0,1,2,3 \qquad (8)$$

Each one of these regions has a width of 4 μm, reaching a total area of 16 μm from the edge. The values of traps concentration and standard deviations for the first region (m=0) are shown in the table below.

Table 3.1: *Parameters for Traps section in the command file of SDEVICE. [49][53].*

Type	Energy (eV)	E_S (eV)	σ_e (cm^2)	σ_h (cm^2)	N (cm^{-3})
e neutral	Ec	0.035	$1.0\cdot10^{-10}$	$1.0\cdot10^{-12}$	$1.0\cdot10^{21}$
e neutral	Ec	0.1	$1.0\cdot10^{-10}$	$1.0\cdot10^{-12}$	$4.0\cdot10^{16}$
h neutral	Ev	0.035	$1.0\cdot10^{-12}$	$1.0\cdot10^{-10}$	$1.0\cdot10^{21}$
h neutral	Ev	0.08	$1.0\cdot10^{-12}$	$1.0\cdot10^{-10}$	$2.5\cdot10^{15}$

3.2.2.2 Radiation damage model

To model the radiation damage in silicon detectors we have implemented a modified version of the Perugia traps model [51] in collaboration with the University of Glasgow [52]. Perugia traps model adopted a simplified approach in which only a reduced set of dominant defects had been considered. For n-type, this reduced set consisted of three levels composed by two acceptor levels, corresponding to di-vacancies V_2 and the V_2O complex, and one donor level, corresponding to traps due to Oxygen and Carbon.

Table 3.2: *Parameters of the trap section for Perugia traps model [51].*

Type	Energy (eV)	Trap	σ_e (cm^2)	σ_h (cm^2)	η (cm^{-1})
Acceptor	Ec-0.42	V_2	$2.2\cdot10^{-15}$	$1.2\cdot10^{-14}$	13
Acceptor	Ec-0.50	V_2O	$5.0\cdot10^{-15}$	$3.5\cdot10^{-14}$	0.08
Donor	Ev+0.36	C_iO_i	$2.0\cdot10^{-18}$	$2.5\cdot10^{-15}$	1.1

The fact of having chosen these energy levels, see table 3.2, is owing to the reported energy levels commonly related to di-vacancies defects. This experimental range is Ec-0.42 eV to Ec-0.55 eV [51] and the best results in simulations were obtained using the energy levels of table 3.2.

The simulated leakage current curves using the Perugia trap model present the right behavior, also the estimated radiation damage constant α is in agreement with the experimental values, which lie in the range 2-10 $\cdot10^{-17}$ A/cm [35]; the depletion voltages match to experimental results [54], CCE curves are also well reproduced. However, trapping times do not match experimental results [55]. This is the reason of a modified version of the trap model [52]. These modifications were realized by altering the cross-sections, to reach the accurate values for carrier trapping, while keeping σ_h/σ_e constant, for not to alter the space charge, see equations (9), (10).

$$\frac{1}{\tau_{e,h}} = \beta_{e,h}\Phi_{eq} = v_{th}^{e,h}\sigma_{e,h}\Phi_{eq}\eta \tag{9}$$

$$n_{e,trap} = N_{trap} f_n \approx N_{trap} e^{-\frac{E}{kT}}\left(\frac{n}{n_i} + \frac{\sigma_h v_{th}^h}{\sigma_e v_{th}^e} e^{-\frac{E_t}{kT}}\right) \tag{10}$$

where the effective trapping probability ($1/\tau_{e,h}$) increases linearly with the fluence (Φ_{eq}), the slope is denoted β, which is given by the thermal velocity of drifting carriers, v_{th}, the carrier capture cross section, σ_{th}, and the introduction rate of defects, η. The results match experimental data and now trapping times are fit to measured trapping times, as shown in table 3.3 [55]. The parameters of this modified trap model are listed in table 3.4.

Table 3.3: *Comparison of calculated β values using model and measured values for the β parameter [55].*

Calculated values from n-type model
$\beta_e = 5.3\cdot10^{-7}$ cm^2/s
$\beta_h = 0.45\cdot10^{-7}$ cm^2/s

Experimental trapping times for n-type silicon
$\beta_e = 4.0\cdot10^{-7}$ cm^2/s
$\beta_h = 5.3\cdot10^{-7}$ cm^2/s

Table 3.4: *Modified parameters of trap section [52].*

Type	Energy (eV)	Trap	σ_e (cm^2)	σ_h (cm^2)	η (cm^{-1})
Acceptor	Ec-0.42	V_2	**$1.5\cdot10^{-15}$**	**$0.9\cdot10^{-14}$**	13
Acceptor	Ec-0.50	V_2O	$5.0\cdot10^{-15}$	$3.5\cdot10^{-14}$	0.08
Donor	Ev+0.36	C_iO_i	**$2.5\cdot10^{-18}$**	**$3.1\cdot10^{-15}$**	1.1

The effect of charge build up at the Si/SiO$_2$ interfaces under irradiation is taken into account by defining a different charge oxide concentration in non-irradiated ($4\cdot10^{11}$ cm^{-3}) and irradiated (10^{12} cm^{-3}) devices respectively [51].

3.2.3 Results

At first place we did a study on the electrostatic potential and the electric field inside the simulated edgeless detector. In figure 3.6 we can appreciate that the isopotential lines are uniformly distributed from the bottom (120 V) to the top (ground) but they present slope when they get closer to the current terminating structure, due to the simulated sawcut defects.

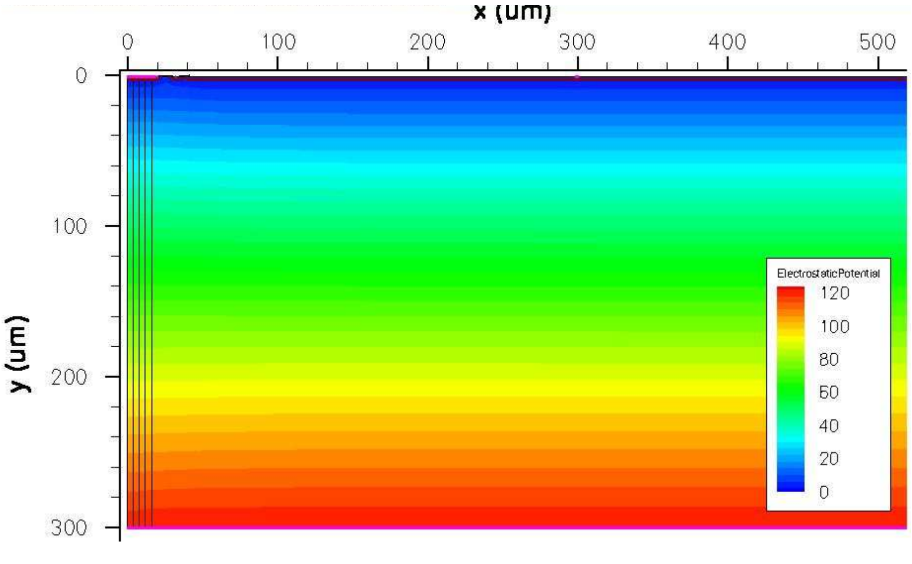

Figure 3.6: *Electrostatic potential distribution in the bulk.*

In figure 3.7 it can be seen a comparison of the Electrostatic potential profile obtained for cuts along the edge of the detector (x = 0) and along an inner position sufficiently separated from the edge (x = 400 μm). Both of them have the curved behavior corresponding to the Poisson's equation (11).

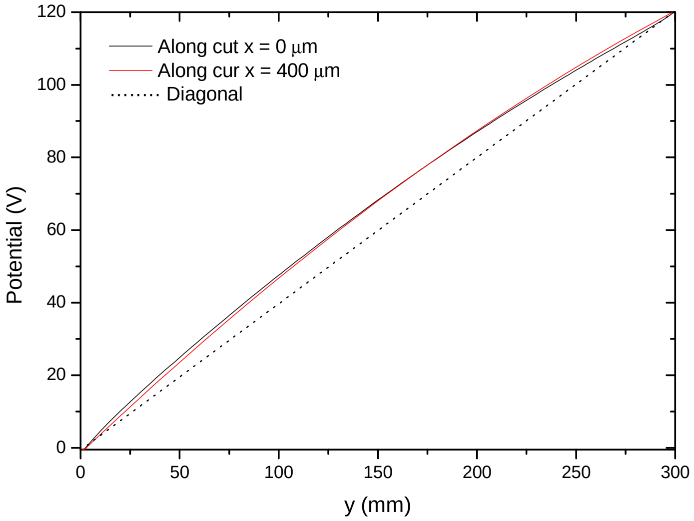

Figure 3.7: *Electrostatic Potential along the detector x = 0 and x = 400 um.*

$$\nabla^2 \varphi = -\frac{qN_{eff}}{\varepsilon_0 \varepsilon_{Si}} \tag{11}$$

The derivation of the electrostatic potential gives us the electric field (see figures 3.8 and 3.9), which experiments a linear growing gradient from the bottom. In those figures we can appreciate the high peak values of the electric field in the edges of the electrodes (CTR, GR and STRIP) due to the increasing in the density of electric field lines. At the top and bottom of the CTR there is also an increasing of the electric field that is caused by the junctions p^+n and nn^+ created by the space charge concentrations, positive and negative, near the n^+ and p^+ contacts, respectively, due to the trapping of carriers of the midgap energy levels of the diamond sawcut induced defects [56].

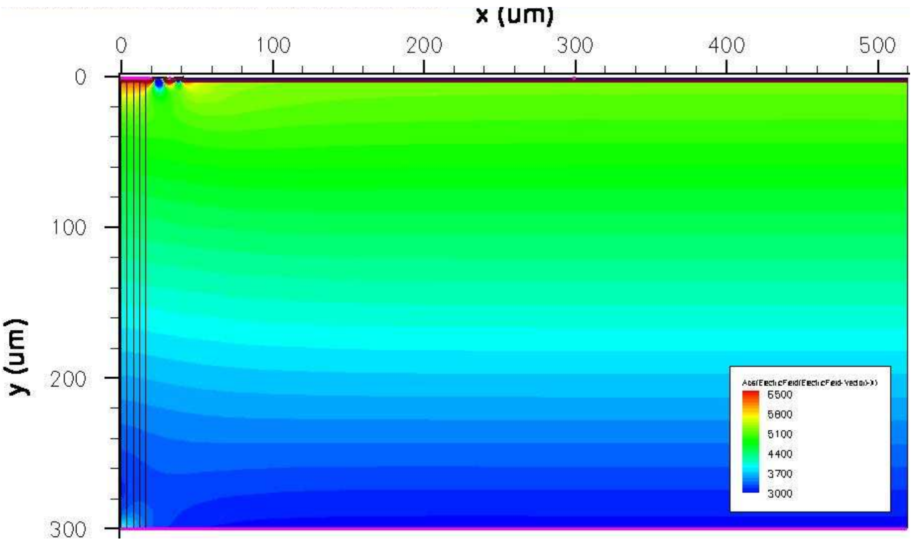

Figure 3.8: *Electric field distribution in the bulk.*

Figure 3.9 shows the curves corresponding to the profile of the Electric Field of cuts along x = 0 and x = 400 µm. Those curves are not flat because of the biasing voltage and their slopes do not start at 0 V/m for being overdepleted. We can also appreciate two vertical peaks (a few micrometers) near 0 and 300 µm, which are produced by the metal-semiconductor junctions.

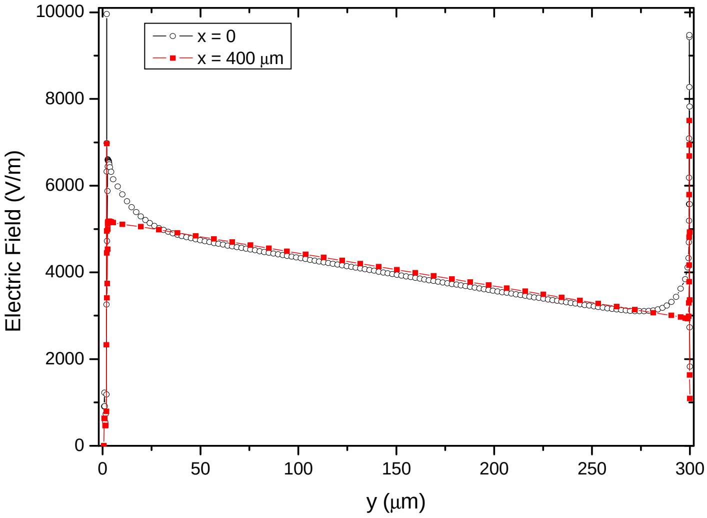

Figure 3.9: *Electric field cut along the edge (x = 0) and x = 400µm.*

The electron and hole current densities obtained using this model can be found in Fig. 3.10. Simulations were carried out applying a bias voltage of 120 V. The results reveal that most part of the generated current due to the high concentration of traps flows through the CTR, and only a small part flows through the GR.

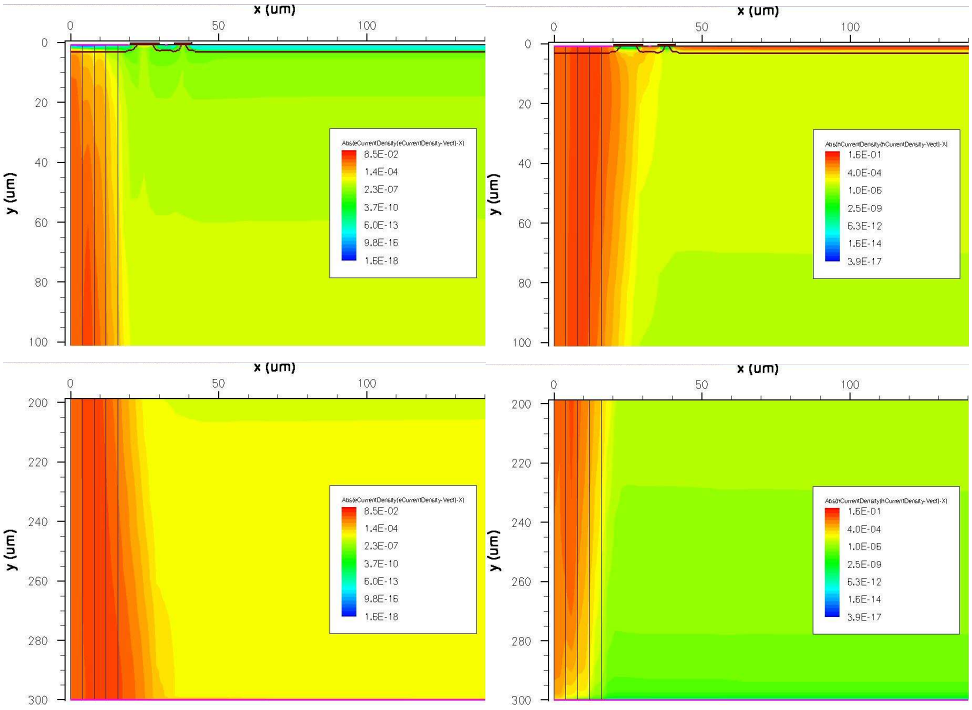

Figure 3.10: *Electron current density (left) and hole current density (right) biasing the detector at 120 V.*

Simulated currents collected at the electrode contacts for different fluences are shown in the figures 3.11-13. In these graphs the currents of the different electrodes biasing the detector up to 120V are shown. The simulation shows that the current at the CTR electrode decreases as the fluence increases, while the GR and the STRIP currents increase with the irradiation fluence, keeping the bias set to 120V in all cases. Figure 3.14 shows the STRIP currents for several fluences under a bias voltage up to 500V, which is the maximum operational bias set for SLHC [9].

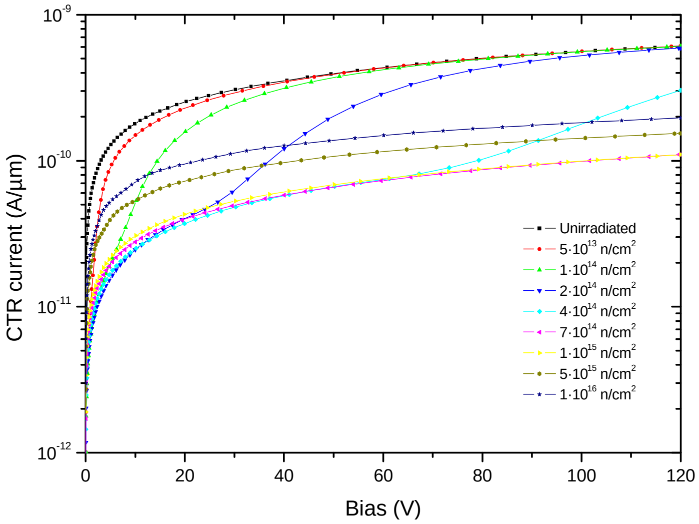

Figure 3.11: *Collected current at the CTR up to 120V.*

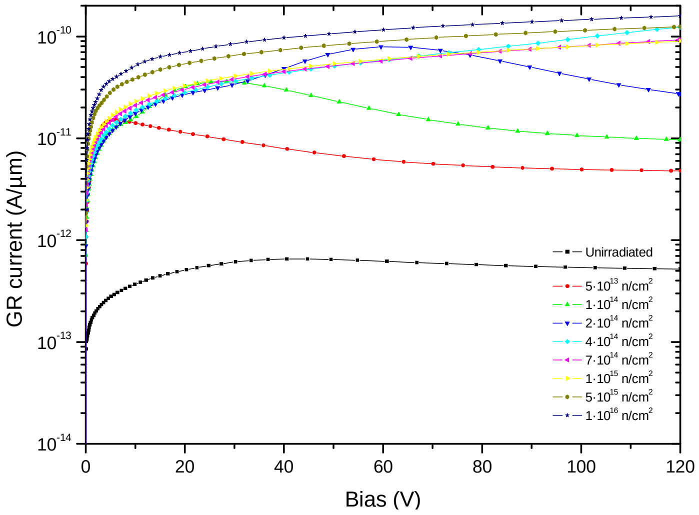

Figure 3.12: *Collected current at GR (guard ring) up to 120V.*

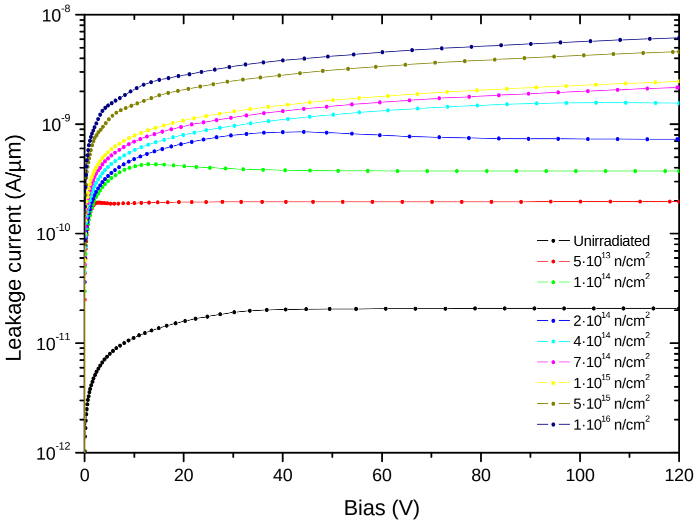

Figure 3.13: *Collected leakage current (STRIP electrode) up to 120V.*

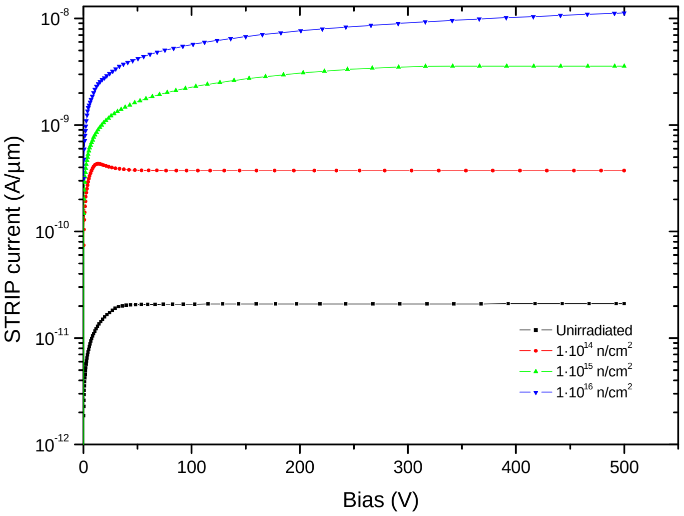

Figure 3.14: *Collected leakage current (STRIP electrode) up to 500V.*

Until this point, we have studied properties of the unirradiated edgeless detectors that have been simulated in this work. The next step consists on the simulation of the irradiated detector at different fluences.

The variation of the electric field at the two edges of the device with the fluence is shown in figures 3.15 and 3.16 respectively. It can be seen in both plots that the increasing of the fluence beyond the type inversion (at a constant bias of 120V) produces a growth of the undepleted region (Electric field equal to zero). As it was said in section 2.1.5, after the type inversion the high electric field is switched from the structured side to the back side of the detector, and so the type inverted bulk is turned an undepleted region with low electric field. Higher and higher biasing voltages are needed to reach a fully depleted detector for growing fluences from the “inversion fluence” (see figure 3.17).

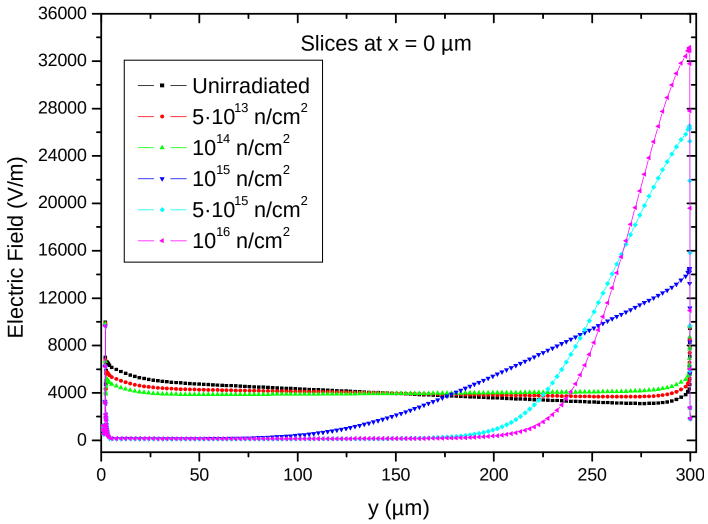

Figure 3.15: *Electric field cut along the edge (x = 0 µm) biasing the detector at 120V.*

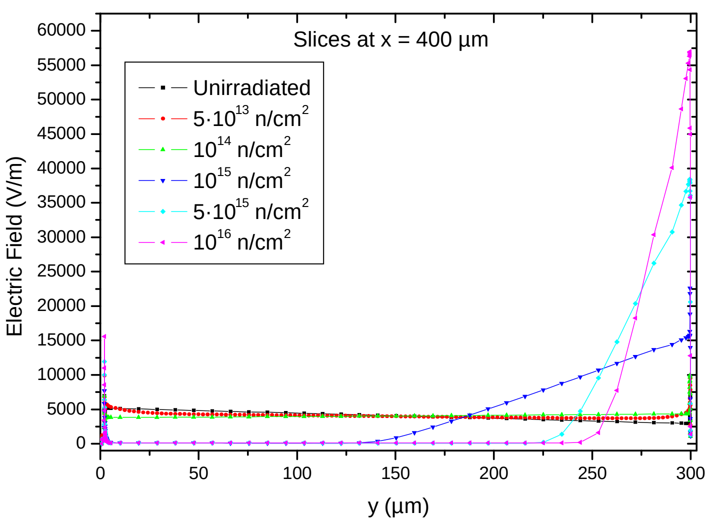

Figure 3.16: *Electric field cut along the edge (x = 400 µm) biasing the detector at 120V..*

Figure 3.17 shows the variation of the full depletion voltage of the detector as a function of the fluence. The full depletion voltage of each measurement was obtained from the CV characteristic applying the LogC-LogV method. This picture also shows that the detector presents bulk type inversion[2] at a fluence of 10^{14} n/cm^2.

---

[2] See section 2.1.2

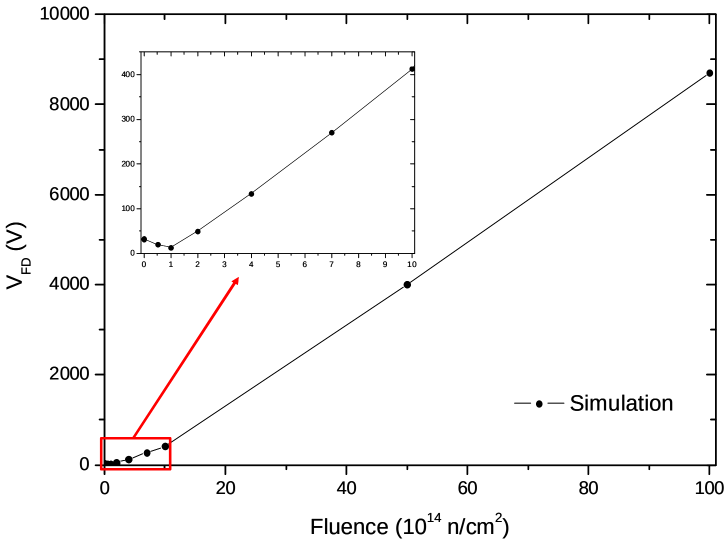

Figure 3.17: *Full depletion voltage as a function of the fluence.*

The estimated leakage current constant α = $2.35 \cdot 10^{-17}$ A/cm^3 is in agreement with the reported experimental values, which lie in the range 2 – $10 \cdot 10^{-17}$ A/cm^3 [35]. This result is taken at room temperature and without annealing, while the universal constant α = $3.99 \cdot 10^{-17}$ A/cm^3 is obtained after 80 minutes at 60ºC [35]. This constant is obtained applying Eq. (5) (see section 2.1.4) to the variation of the leakage current after irradiation per detector volume unit as a function of the neutron equivalent irradiation fluence. These leakage currents are achieved at full depletion voltage for the corresponding irradiation fluence.

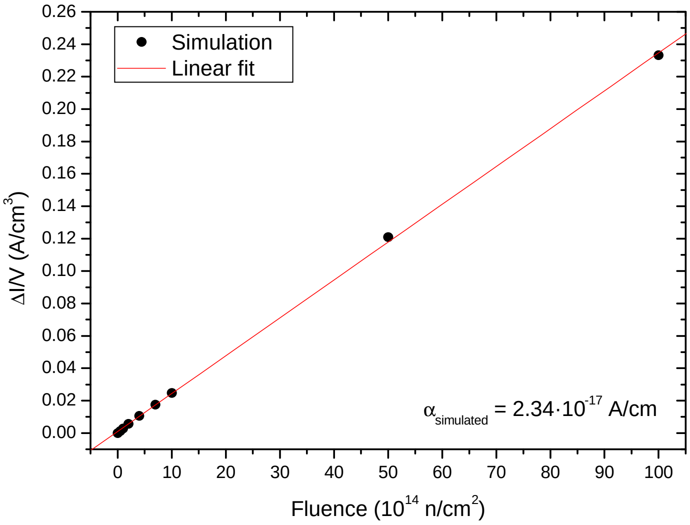

Figure 3.18: *Simulation of the increment in leakage current density as a function of the fluence.*

Next step consisted in studying the response of edgeless detectors to tracking particles. To carry out this task several tracks of particles have been introduced in the detector from the edgeless side to obtain information about the different areas of the detector for different irradiation fluences.

In figure 3.19 the position of the different tracks of the minimum ionizing particles (mip) used to simulate the charge collection efficiency at different irradiation fluences are shown. The chosen positions for the tracking of particles were at 10, 30, 50, 100 and 250 µm from the edge side.

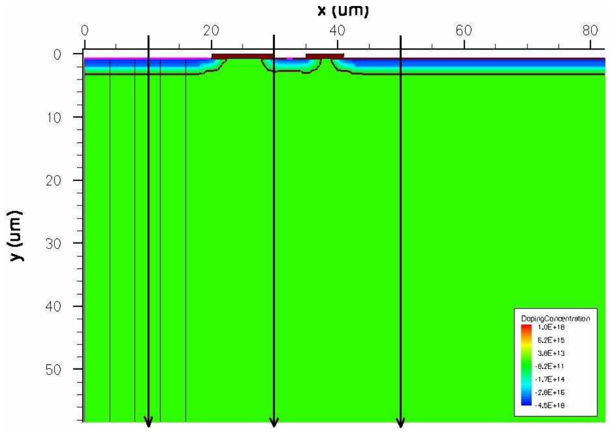

Figure 3.19: *MIP traces at 10, 30 and 50 microns from the edge side.*

The MIP simulated by Sentaurus Device software consisted on a particle track, created using the HeavyIon command, in vertical direction which has a Gaussian shape with a width of 1 µm. The charge generated along the MIP track is 80 pairs electron-hole per µm, covering the whole thickness of the detector. Figures 3.20 shows the hole current density for an irradiated detector at $7{\cdot}10^{14}$ n/cm^2 for a MIP crossing at 100 µm from the edgeless side biased at 120V. Some frames have been taken at 0.05, 1.2, 4, 15, 25 and 50ns. It can be appreciated the asymmetrical distribution of the charge cloud which is balanced to the inner region of the detector.

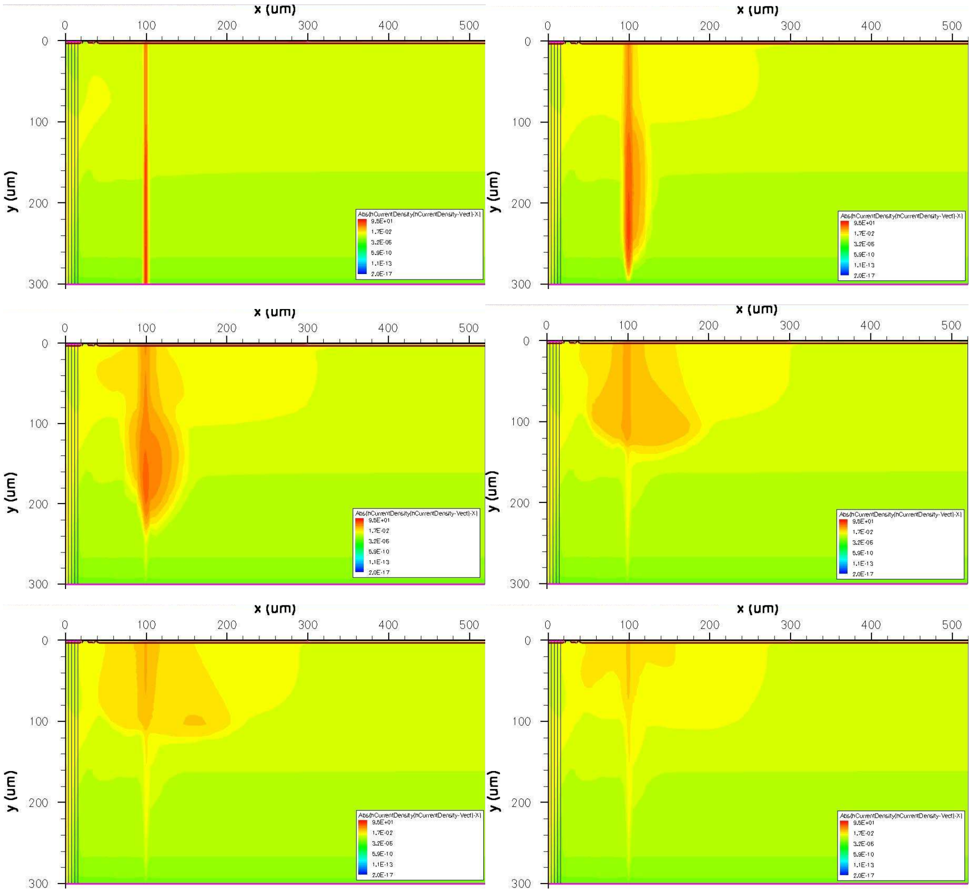

Figure 3.20: *Holes current density distribution in the bulk for a mip track at 100 μm from the edgeless side. The irradiation fluence was* $7{\cdot}10^{14}$ *n/cm*^{2}.

Figure 3.21 contains the charge collection efficiency (CCE) curves for the simulated detector using mip particles crossing at different positions, for different irradiation fluences. These CCEs, which corresponds to the STRIP electrode, have been obtained biasing the detector at 120V and for integration time set to 75ns. As expected, the efficiency decreases as the fluence increases due to the increment of charge traps in the bulk.

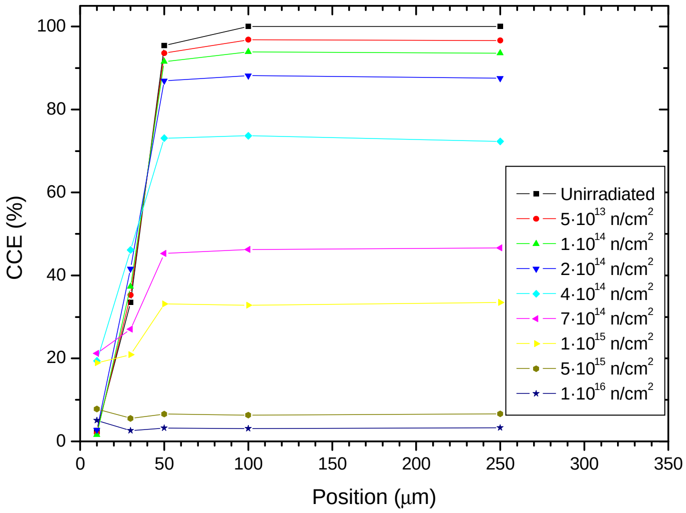

Figure 3.21: *Charge collection efficiencies of the detector depending on the mip crossing position for an integration time of 75ns biasing the detector at 120 V for different fluences.*

Charge collection efficiencies obtained using an integration time of 25 ns and a 120 V bias are shown in figure 3.22. Comparing figures 3.21 (integration time 75 ns) and 3.22 (integration time 25 ns) there are not appreciable differences for fluences below $2 \cdot 10^{14}$ (radiation defects are not yet important enough) and above 10^{15} n/cm^2 (the 120 V applied bias is insignificant compared to the full depletion voltages which reach several thousands volts). In the range $2 \cdot 10^{14}$ – $1 \cdot 10^{15}$ n/cm^2 the combination of the radiation damage and the applied bias, which make the detector be partially depleted for these fluences, makes appreciable some differences.

In both graphs, for fluences higher than $2 \cdot 10^{14}$ n/cm^2 the detector is underdepleted and consequently part of the charge is lost, so it is needed to increase the bias for these fluences to get results of the charge collection efficiencies where all the curves are obtained fully depleted.

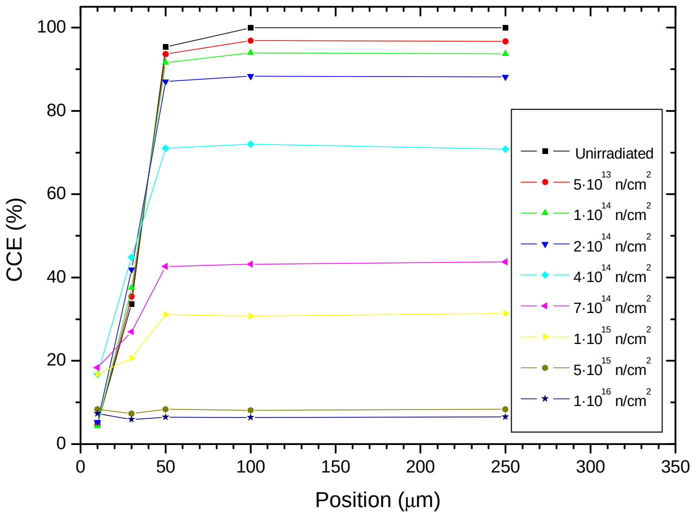

Figure 3.22: *Charge collection efficiencies of the detector depending on the MIP crossing position for an integration time of 25ns biasing the detector at 120 V for different fluences.*

Figure 3.23 presents the results biasing the detector at 120V for lower fluences (up to $2{\cdot}10^{14}$ n/cm^2) while for higher fluences the detector is biased at 500V, this way all of the plotted curves are fully depleted, except the curve for the 10^{16} n/cm^2, whose expected full depletion voltage is around 9000V.

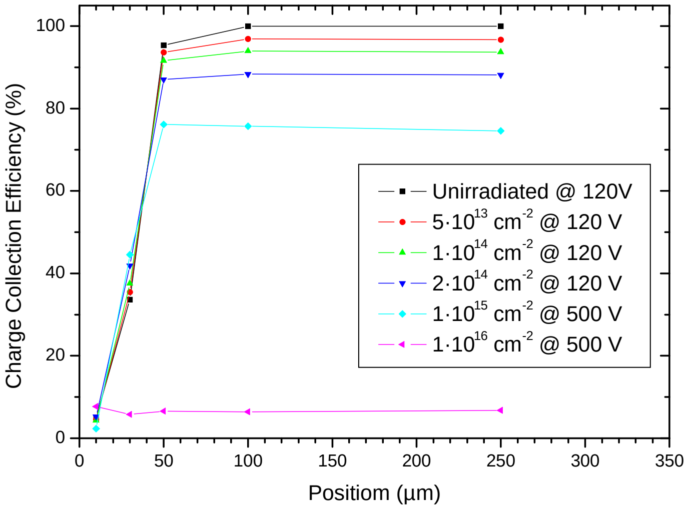

Figure 3.23: *Comparison of Charge collection efficiencies depending on the position for two biasing voltages: 120 V and 500 V. Integration time was set to 75 ns.*

Another aspect to take into account is the increasing of the CCE for particles crossing the detector at the CTR (20 microns from the edgeless) for the fluences $4{\cdot}10^{14}$, $7{\cdot}10^{14}$ and 10^{15} n/cm^2. At higher fluences the bias voltage is negligible in front of the full depletion voltage. Figure 3.24 shows the CCE behaviour at different fluences for two regions: CTR (MIP crossing at 10 µm) and a region far away from the edge (MIP crossing at 100 µm). CCE, as expected due to the radiation damage defects, decreases as the irradiation fluence increases, but for 10 µm it takes place an increasing in the CCE up to 20% for fluences were the detector is partially depleted when it is biased at 120V.

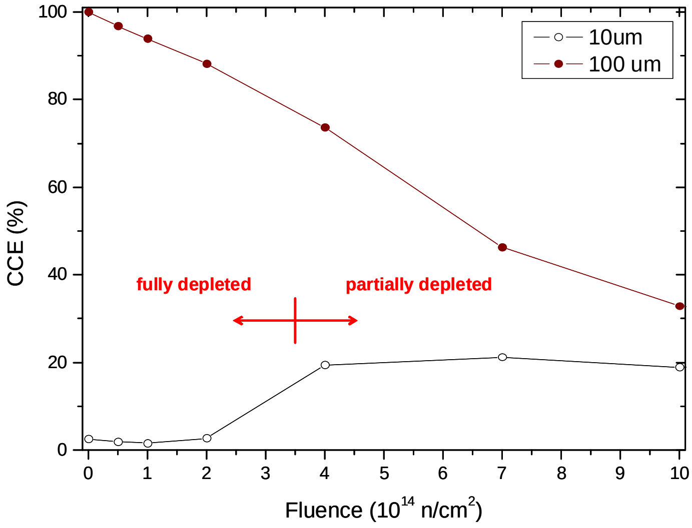

Figure 3.24: *Comparison of charge collection efficiencies depending on the fluence for 2 MIP crossing at 10 and 100 µm biased at 120 V bias. Integration time was set to 75ns.*

To find the explanation of that behavior, the electric field and the hole density distributions were studied. Figs. 3.25 and 3.26 show the electric field distribution for the non-irradiated detector and the irradiated one at $4 \cdot 10^{14}$ n/cm^2 respectively.

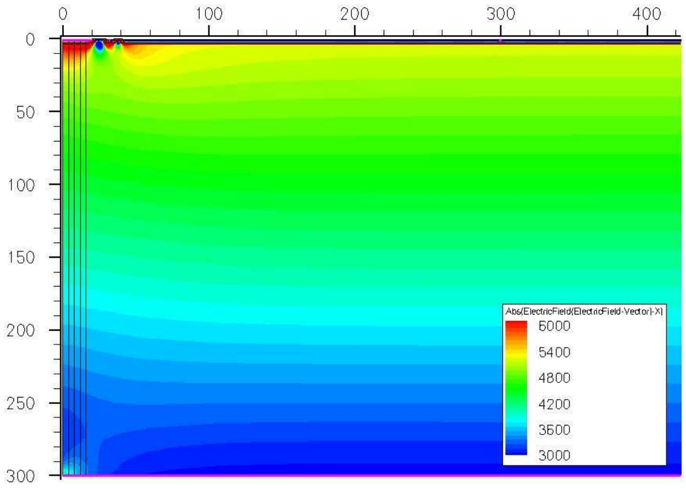

Figure 3.25: *Electric filed distribution of the unirradiated detector biased at 120 V.*

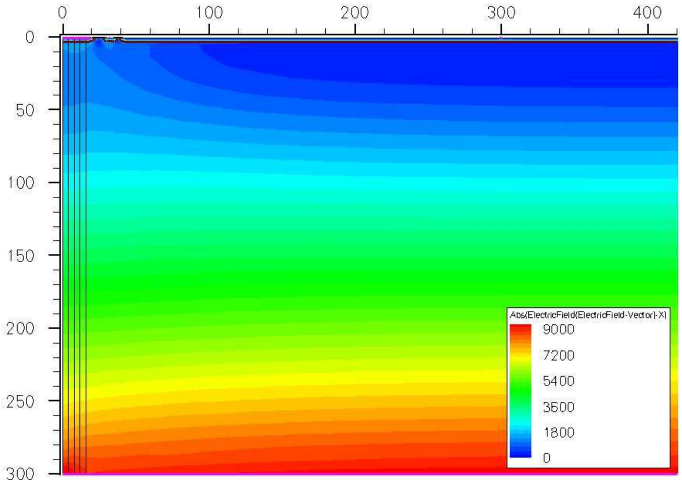

Figure 3.26: *Electric field distribution of the detector irradiated at $4 \cdot 10^{14}$ n/cm^2 biased at 120 V.*

In the unirradiated detector the electric field located at the current terminated ring (CTR) is higher and the generated charge by the impinging mip particles at 10 μm will be mostly collected to the CTR electrode. In the other hand, the irradiated detector, which is partially depleted, does not present so high difference in the electric field between the CTR and the strip electrodes, and a small part of the charge (20%, see Fig. 3.24.) is collected by the strip electrode.

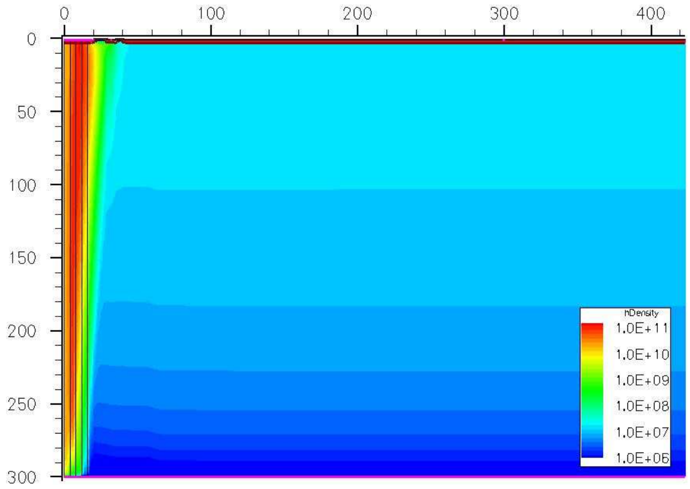

Figure 3.27: *Hole density distribution of the non-irradiated detector biased at 120 V.*

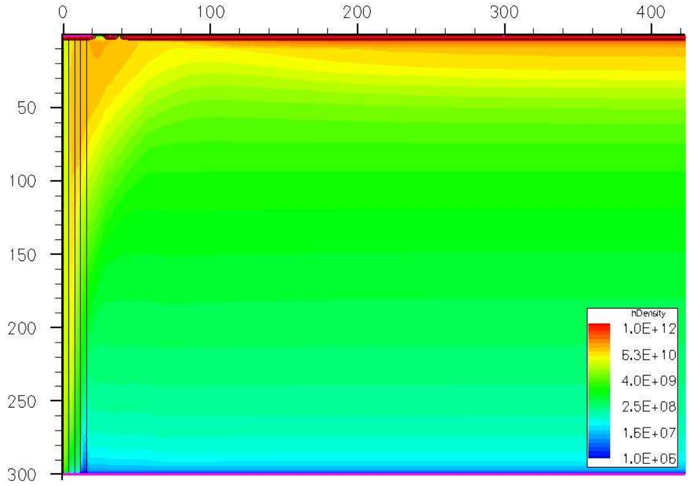

Figure 3.28: *Hole density distribution of the detector irradiated at* $4{\cdot}10^{14}$ *n/cm*^{2} *biased at 120V.*

Through the comparison of the hole density distributions of the detector in both cases (figures 3.27 and 3.28 respectively), it can be said that the degradation of the detector by irradiation produces charge traps along the detector and, if the detector is not fully depleted, a part of the charge generated by the impinging mip can be deflected to the strip electrode.

3.3 Conclusions

In this work, irradiated edgeless detector structure developed by the TOTEM collaboration has been described and simulated. Two different sets of deep levels, one for the diamond saw cut and one for the radiation damage, were implemented and combined to simulate the behavior of edgeless detector at different fluences.

The models show that throughout most of the device, the charge collected after radiation damage is the same as standard p-on-n strip detectors with full guard ring structures. Biasing the detector at the same potential (120V) and extending the integration time (25 to 75 ns) it was found that for high fluences, which lead to partial depletion of the detector for this bias, the integration time becomes essential factor for the CCE.

Besides, it was found an increase of the charge collected on the strip electrode for partially depleted irradiated detectors, when the charge is generated by particles passing through the CTR structure. This is suppressed by increasing the bias for the high irradiation fluences to restore the fully depletion condition. Taken this into account, a maximum bias of 500V is enough to guarantee this condition up to an equivalent fluence of 10^{15} n/cm^2.

4 Simulation of ultra thin 3D silicon detectors

A novel ultra thin silicon detector called U3DTHIN has been designed, simulated and fabricated for applications that range from neutral particle analyzers (NPA) used in Corpuscular Diagnostics of High Temperature Plasma to very low energy X-Ray spectroscopy. The main purpose of this detector is to provide a state-of-the-art solution for the upgrade of the current detector system of the NPAs at JET and also to pave the road for the future detection systems of the ITER experimental reactor. Currently the NPAs are using very thin scintillator - photomultiplier tube, their main drawbacks are poor energy resolution, intrinsic scintillator nonlinearity, and relative low count rate capability and finally poor signal-to-background discrimination for the low energy channels. This new U3DTHIN detector is based on columnar electrodes passing through a very thin sensitive substrate which will provide nearly 100% detection efficiency for ions and at the same time very low sensitivity for the neutron and gamma background.

4.1 Potential applications

One of the most innovative features of this novel 3D ultrathin detector is the optimal combination of the thin entrance window and the sensitive substrate thickness, which will make possible to accommodate very large dynamic range of detected ions. A series of potential applications in which this novel ultra thin 3D detector can be used is listed below.

4.1.1 High temperature plasma diagnosis for the ITER fusion reactor

The increase of power of the plasma shots in the JET tokamak has brought significant problems for the operation of the Neutral Particle Analyzers (NPA) detector systems. This type of diagnostics is used to perform Corpuscular Diagnostics of plasmas. The increase of the plasma burning power has risen the neutron and gamma background in such a way that detectors can not cope with the particle rate. Therefore these detectors get saturated and are not able to detect ions from the plasma, which carry information about the plasma parameters. It is very well known that this problem will be even more severe in the new generation of tokamaks. One of these will be installed in the ITER facility. In order to provide a detector capable to detect ions under such high intensity of neutrons and gamma background we introduce a device with novel concept using an ultra thin silicon detector with 3D electrodes.

4.1.2 Neutron detection [57]

There are several methods by which neutrons may be produced in the fuel cycle, the basic principles are the following:

- **Alpha particle induced reactions**

  Plutonium and uranium isotopes decay by alpha particle emission. The alpha particle is absorbed by the nuclei of the low atomic number elements (Li, B, Be, O, F, C, Si, etc.) and a neutron is produced. The yield depends upon the chemical composition of the matrix and the alpha production rate for plutonium and uranium. Neutrons from (α,n) reactions are produced randomly (not time-correlated) and they exhibit a broad energy spectrum. Other α-emitting nuclides can also make important contributions, for example ^{241}Am.

- **Spontaneous fission**

  The even-numbered isotopes of plutonium (^{238}Pu, ^{240}Pu, and ^{242}Pu) spontaneously fission (SF) at a rate of 1100, 471, and 800 SF/gram-second respectively. Like (α,n) neutrons, SF neutrons have a broad energy spectrum. SF neutrons are time-correlated (several neutrons are produced at the same time), with the average number of neutrons per fission being between 2.16 and 2.26. Uranium isotopes and odd-numbered plutonium isotopes spontaneously fission at a much lower rate (0.0003 to 0.006 SF/gram-second). In spent fuel Cm and Cf isotopes may be significant.

- **Induced fission**

  Fissions can be induced in ^{239}Pu, ^{235}U, and ^{238}U by neutron interrogation of the sample with an external neutron source. Like SF neutrons, they have a broad energy spectrum and are time-correlated.

The neutron detection is mainly carried out by the properties of the neutrons, which have mass but no electrical charge. Because of this, they cannot directly produce ionization in a detector, and therefore can not be directly detected. This means that neutron detectors must rely upon a conversion process where an incident neutron interacts with a nucleus to produce a secondary charged particle. These charged particles are then directly detected and from them the presence of neutrons is deduced.

The most common reaction used for high efficiency thermal neutron detection today is:

$$n + {}^{3}He \rightarrow p + {}^{3}H + 765\ keV$$

Where both the proton and the triton can be detected by the U3DTHIN using a polyethylene converter on top of the detector.

Another common method uses ^{10}B atom in the converter, in which fission of the atoms will provide the charged particle.

$$n + {}^{10}_{5}B \rightarrow \begin{cases} \alpha + {}^{7}_{3}Li + 2.310\ MeV\ (94\%) \\ \alpha + {}^{7}_{3}Li + 2.792\ MeV\ (6\%) \end{cases}$$

Such an instrument configuration can be used as the one presented in figure. 4.1 with and added layer of Boron on top.

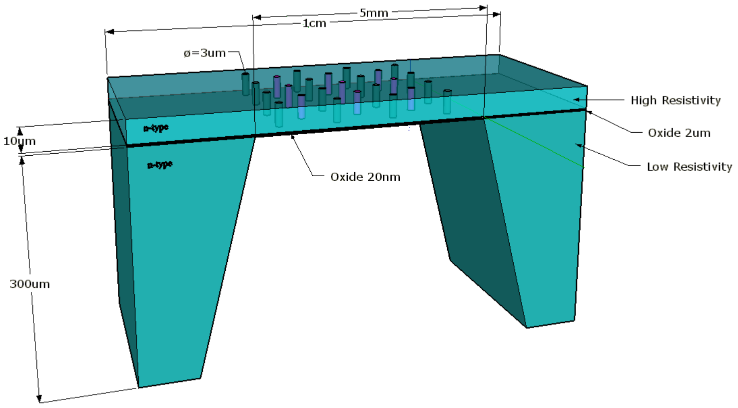

Figure 4.1: *A schematic layout of the diagnostic sensor station based on ultra thin 3D silicon detectors (U3DTHIN)*

This is usually done by surrounding the detector and/or the sample being counted by a hydrogen-rich material (moderator) such as high density polyethylene. Typically 10 cm of polyethylene surround the detector.

Note that there is no *apriori* information about the primary neutron spectrum. Since all of the neutrons which are detected have been moderated, to reduce their energy to the thermal level, all neutron energy information is lost. All of the events of interest fall into the peak 765 keV, which is the reaction energy. Once a discriminator has been set to eliminate the gamma interference and those events produced by interactions with the walls of the detector tube, simple gross counting is all that is required.

4.1.3 Low energy x-ray detection [58]

The investigation of X-ray fluorescence at low excitation energy is a growing research due to the present availability of synchrotron light sources of high brilliance.

The X-ray absorption spectrum of atoms can provide information about the detailed structure of matter which is of interest in several related fields like material science and biophysics. Experiments like Extended X-ray Absorption Fine Structure (EXAFS) and X-ray Absorption Near Edge Structure (XANES) typically require a detection system able to measure low-energy X-rays within energy range from 2 to 10 keV, with high energy resolution, operating with high count rates and with very high radiation hardness.

Complementary to this; the X-ray soft emission from gas plasma can be one potential application. In this application the emission spectra for the X-rays lays within a range between 0.1 – 15 keV.

4.1.4 High energy x-ray and gamma ray detection [59]

For X-ray spectroscopy and scintillation light collection, the most important characteristic of U3DTHIN is the small capacitance of the collecting anode (of the order of 10 fF), due to its small surface. Moreover, this capacitance is independent of the active area of the device. This is the main advantage of an U3DTHIN with respect to a p-i-n photodiode (PD) with the same active area and thickness, which its collecting anode extends over all the detector surface, and thus exhibits a much higher capacitance.

As the detector capacitance originates one of the major noise components in a radiation detector system, a reduction in capacitance will give rise to lower noise and thus to better energy resolution performance. Moreover, the first transistor of the pre-amplifying electronics can be directly integrated on the same detector's chip. The transistor integration on the device allows fine capacitive matching with the detector and reduces to a minimum any stray capacitance due to connections, thus further reducing the electronic noise. U3DTHIN have been designed also as X-ray detectors, allowing high spectroscopic performance even at room temperature. Better performance can be obtained with moderate cooling, for example by means of a Peltier cooler.

The U3DTHIN will be optically coupled to CsI(Tl) scintillating crystals for gamma ray detection. In this configuration the energy range is limited by the crystal thickness and by crystal geometry and wrapping considerations, but a several hundreds keV are easily achievable.

4.1.5 Low energy heavy ions [60]

The detection and the measurement of low energy fluxes of ions are of great importance in research involving charged particles. The commercially available detectors of comparable size to U3DTHIN for this purpose like channel electron multipliers (CEM) are more costly and in many of these devices the electronics circuits are placed in vacuum chambers, which reduce their maneuverability, and the probability of failure due to pressure surges in the vacuum system is increased. The need for detection of low energy flux of ions arose during the development of direct recoil spectroscopy and the twin detection techniques, i.e. ion induced photoemission – secondary mass spectroscopy. One decision could be the use of passive detectors like plastic scintillators to make an attempt to circumvent some of these problems. Plastic scintillators are widely used in the detection and spectroscopy of charged particles (electrons, H+, He+) and neutral radiation (neutrons, gamma, X-rays) in the energy range of MeV. A typical mass resolution of 0.25 a.m.u. between ^{1}H and ^{2}H isotopes of energies 400 MeV/n in the cosmic ray. Plastic scintillators have been tested to detect low energy X-rays and gamma rays. A low energy limit of 3–4 keV is achieved for the detection of gamma rays. Our attempts to study the detection response of U3DTHIN by bombardment of heavy species C^+70, C^+60, C^+24, Xe^+2 , Xe^+ and Ar^+ in the energy range of 1–10 keV. The response time of U3DTHIN would be of 1 ns, which is comparable with most channel electron multipliers.

4.1.6 Other applications

Other potential applications for the U3DTHIN could be those where is needed high count rate and radiation hardness such are for the Compton electrons suppression and for the Trigger of Low Energy Heavy Ions.

4.2 Detector layout design

To achieve very fast collection of charge carriers generated by the incident ions, a 3D electrode structure [61] has been introduced in the sensitive volume of a thin detector. One of the most innovative features of these detector is the optimal combination of the thin entrance window and the sensitive substrate thickness, this will make possible to accommodate very large dynamic range of the detected ions.

Results from GEANT4 and Sentaurus simulations are used to find the thicknesses of the entrance oxide window and the silicon substrate. An entrance window with a thickness of tens of nanometers together with a sensitive substrate thickness varying from less than 5 μm, to detect the lowest energetic ions to 20 μm for the heigher ones, are the optimal choice.

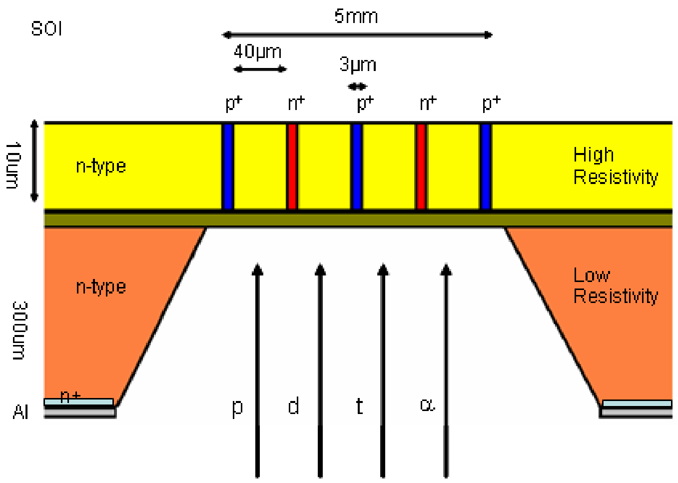

Figure 4.2: *Thick cross-section detector's design. The drawing is not to scale.*

The new detector concept is shown in figure 4.2 and 4.3. This configuration was obtained combining 3D detector technology with thin membrane fabrication process. Since the detector is illuminated from the back side surface, there will be no dead layer where the ions loose energy.

The first set of test structures has already been fabricated in order to prove the viability of the idea. Given the fact that the test structures were successfully fabricated, a new set of devices were ordered to fabricate and currently the are available.

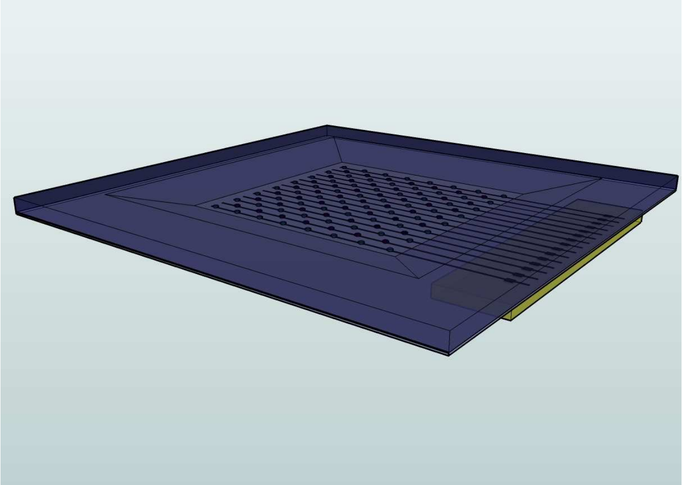

Figure 4.3: *Final layout of ultra thin 3D detector fixed to a read-out electronic chip.*

To increase the signal to background ratio the detector will have spectroscopy capability which will allow performing pulse-height analysis. Preliminary results showing the technology used to fabricate these 3D ultra thin detectors developed at Centro Nacional de Microelectronica in Barcelona will be presented in section 4.4.

4.3 Simulations

Sentaurus simulation software package [46] was used to simulate the electrical characteristics and the technological properties of the 3D-thin detectors in order to find the optimum parameters for the definition of the detector geometry and the fabrication process. In order to keep the size of the simulated mesh as small as possible only a single cell of the device with 4 n^+ columns and 1 p^+ column was simulated, as shown in figure 4.7.

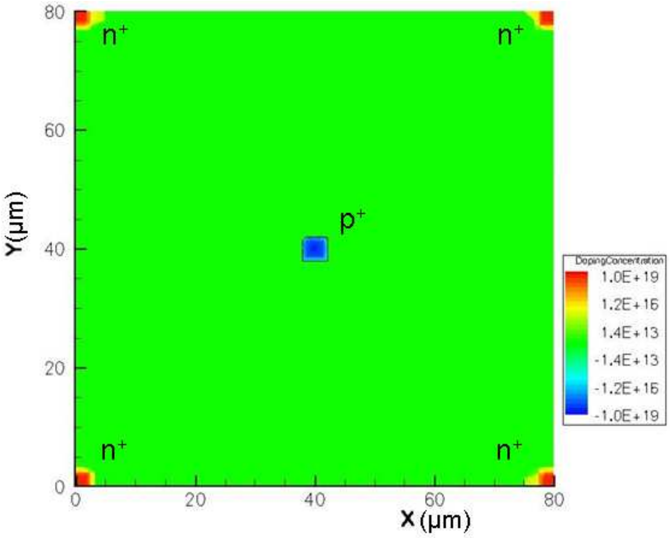

Figure 4.7: *Two-dimensional plot of the square geometrics used for the simulations.*

Because of the device's symmetry, this is sufficient to understand the behavior of a much larger array. In figure 4.8, the simulated device structure is shown. The substrate used was n-type with a doping concentration of 10^{12}

cm^{-3}. In order to increase the radiation hardness of these devices p-type substrates with electron readout could be used as demonstrated in [63].

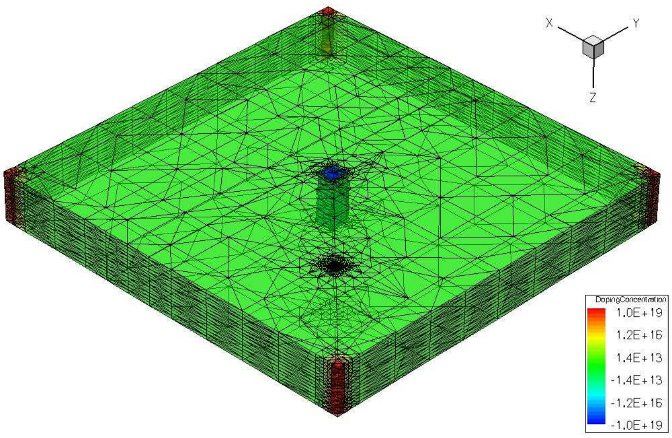

Figure 4.8: *Layout of the simulated device using Sentaurus software package.*

The square pitch was set to 80 µm and hole collection was carried out in the central electrode, doped p-type. The simulated I-V characteristic up to 150 V is shown in figure 4.9.

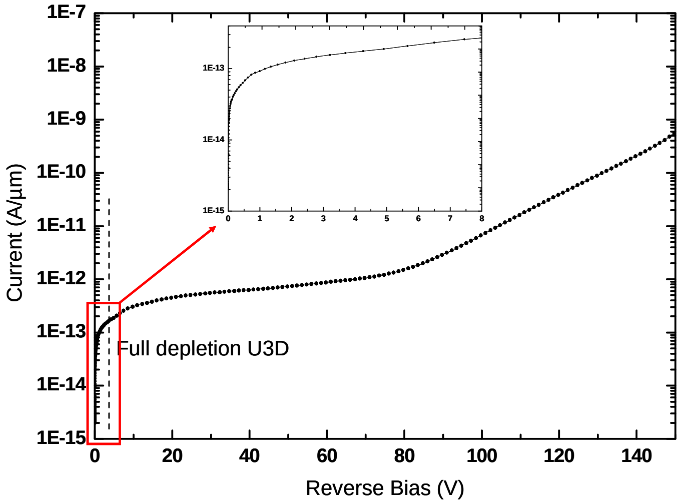

Figure 4.9: *Simulated IV characteristic of the U3DTHIN detector up to 150V.*

The breakdown voltage predicted by the 3-dimensional simulation is around 80 V, enough to fully deplete the detector. The simulated capacitance of the column falls rapidly with increasing voltage as the device depletes. The capacitance saturates at about 3.5 V to a value of 2.5 fF per column. The coaxial cable approximation, which regards the column as being a coaxial cable with radius equal to the distance between n^{+} and p^{+} electrodes, is used to compare 3D-thin detector capacitance to a planar thin device with the same surface area using the standard parallel plate capacitance. Figure 4.10 shows that the 3D-thin capacitance is two orders of magnitude smaller than the one of a planar. However, increasing the thickness this difference is reduced reaching the unity at a value depending on the surface area. For thick detector the capacitance of 3D detector is higher that planar as already predicted [52].

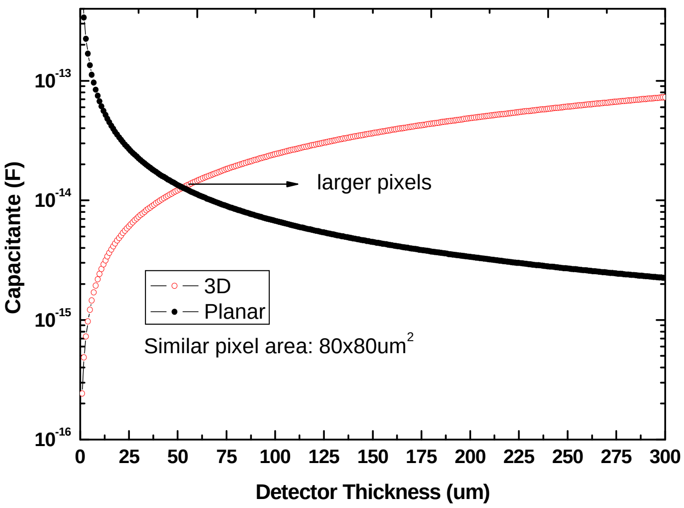

Figure 4.10: *Geometrical capacitance as a function o the thickness of 3D detectors compared to planar detectors with similar surface areas.*

The charge collected at the electrodes has also been simulated with Sentaurus software. If the minimum bias voltage needed to fully deplete the device is used, the collection time is quite long and the signal peaks at 30ns, however increasing the bias to 30 V the signal peak goes down to only 1 ns, as can be seen in figure 4.11. This means that, with a suitable electronics, the count rate of actual devices used in corpuscular diagnostics plasma could be improved beyond 1MHz [62].

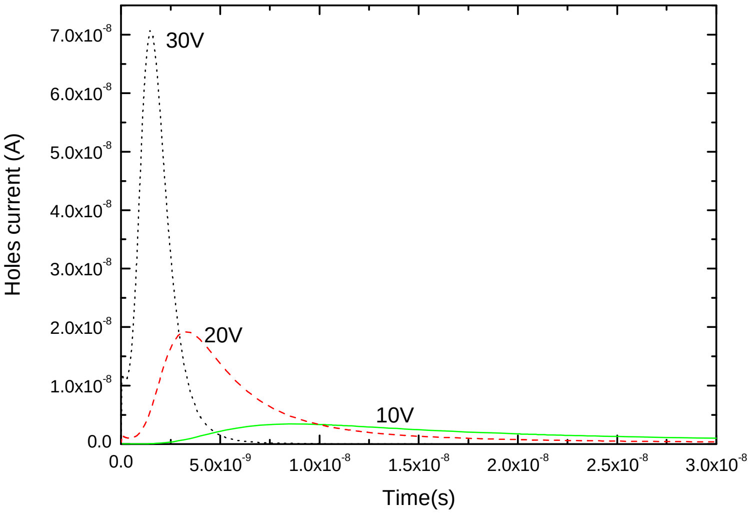

Figure 4.11: *Charge collected at different bias voltages for MIP irradiation. At 10 V the signal peaks at 10 ns but at 30 V the peak is at 1 ns.*

A detailed Geant4 simulation of this optimal parameter was carried out at the Helsinki Institute of Physics (HIP) [62], see figures 4.4, 4.5 and 4.6.

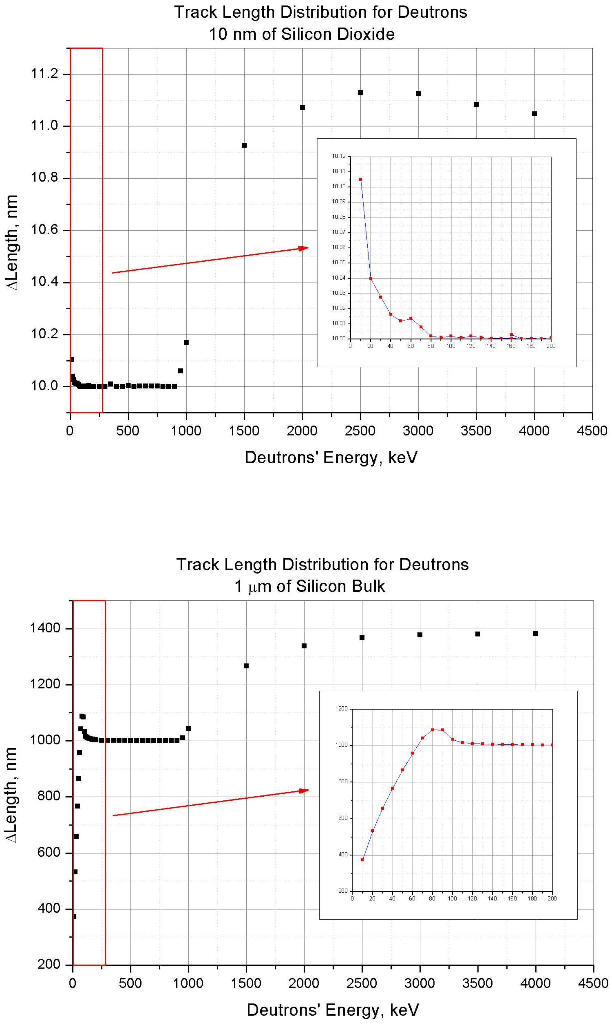

Figure 4.4: *Track Length distribution for Deuterons in the silicon oxide window (up) and the sensitive substrate (down) using GEANT4 [62].*

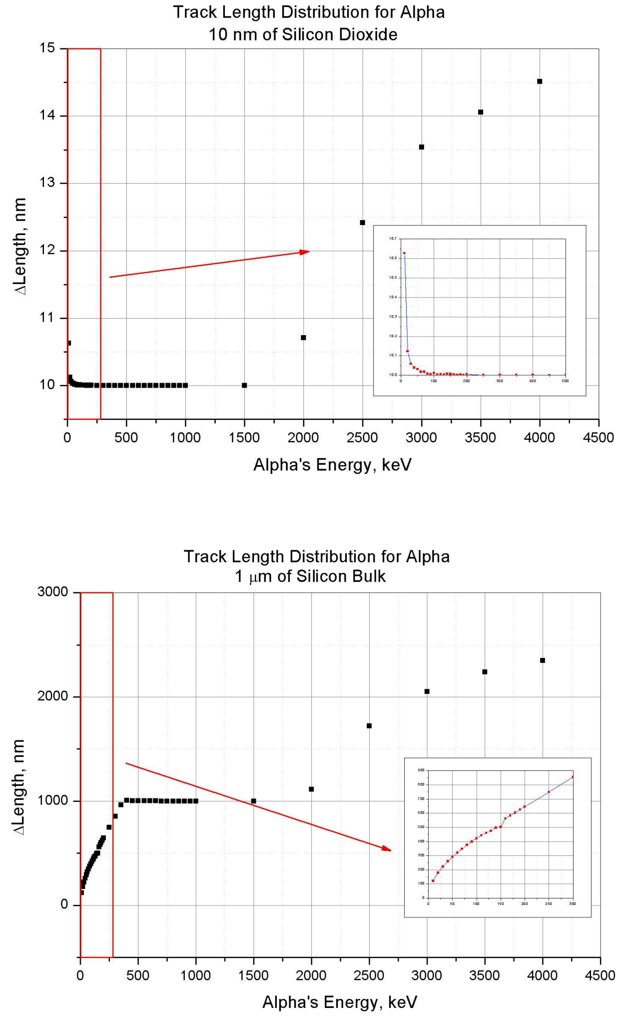

Figure 4.5: *Track Length distribution for Alpha particles in the silicon oxide window (up) and the sensitive substrate (down) for different energies using GEANT4 [62].*

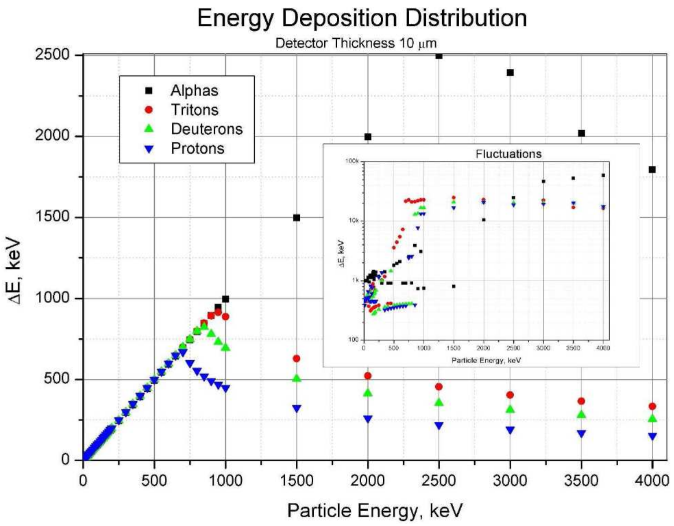

Figure 4.6: *Energy deposition distribution in the sensitive substrate for different particles and energies [62]*

4.3 Feasibility of fabrication

In this work are presented the technological results obtained in the fabrication of these ultra thin 3D detectors. The electrical and technological simulations were used to predict the behavior of this new device. With this information a new mask set was designed which includes different detector geometries: simple pad, strip detectors and test structures.

To test the feasibility of the fabrication of the U3DTHIN detectors a fast test RUN was designed and carried out at the CNM facilities. The fabrication steps are described below [64][65]:

1. **Wafer characteristics.**

For the fabrication of these U3D detectors a SOI wafer was used. The top region is a 10 µm layer of high resistivity n-type Silicon, the insulator is a layer of SiO_2 1 µm thick and the bottom region is 300 µm of n-type low resistivity Silicon.

2. **General cleanliness.**

This step consists on the cleaning of the wafer to remove any organic or metallic remain prior placing them inside the oven, for preventing its contamination. It is also removed the native oxide layer that could be grown at room temperature. This process consists of 10 minutes bath of a mixture of SO_4H_2 and H_2O_2, then a rinsing deionized (DI) water shower, and a 10 seconds bath of HF (10%) to remove superficial oxides. Then the wafer is placed in another rinsing DI water cascades and finally dried by the rinser-dryer to continue the fabrication process.

3. **Wet oxidation (800 nm).**

The wet oxidation consists on submitting the wafer at high temperature within an oxidant atmosphere (oxidant agent: H_2O). This process creates a fresh interface region, with surface contamination on the original silicon ending up on the oxide surface.

4. Standard photolithography.

The Photolitography process transfers the pattern used to define the position of the alignment marks on the mask to a thin layer on the wafer. It is carried out dehydrating the wafer (200ºC, 30 minutes), then a photoresist deposit of 1.2 µm, alignment and proximity illumination at 7 µm, and then the development of the photoresist. After this process is made an annealing to harden the photoresist because of the following wet etching could damage it.

5. Wet etching on the silicon oxide through photoresist.

Used to open windows in the silicon oxide, this mechanism consists on chemical reactions which take place between the oxide and the reactants of the products away.

6. Removal of the photoresist.

The photoresist layer is removed using oxygen plasma.

7. General cleanliness.

A general cleanliness to remove all the products left after the previous steps. The cleaning process is described in 2.

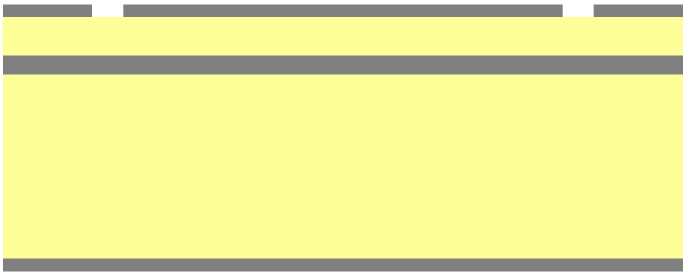

8. Wet oxidation at 1100ºC (400 nm).

Once the widows of the alignment marks are open, a thermal oxidation of the wafer takes place to grow a 400 nm oxide layer, at 1000ºC.

9. Removal of the silicon oxide of both faces.

A bath of SiO etch at room temperature is applied to etch the silicon oxide layers of both faces of the wafer.

10. General cleanliness.

This is the same process that was described in step 2.

11. Wet oxidation (800 nm).

An 800 nm silicon oxide layer is grown at this point. This layer will be the support of the windows that will be used for the electrode columns.

12. Photolithography.

In this step the position of holes for the columns of the 3D detectors on the photoresist are generated. This step is described in step 4.

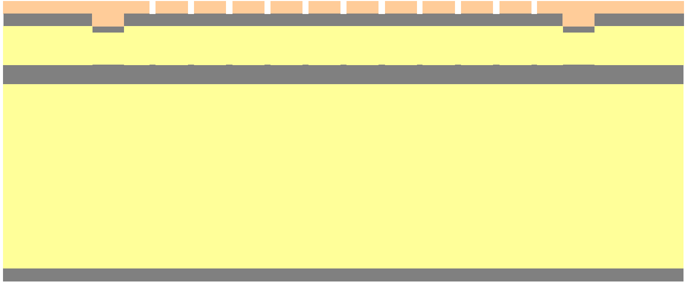

13. Deep Reactive Ion Etching (DRIE).

An Inductively Coupled Plasma (ICP) was used to open the holes in the oxide, 800 nm, as well as in the silicon layer, 10.000 nm.

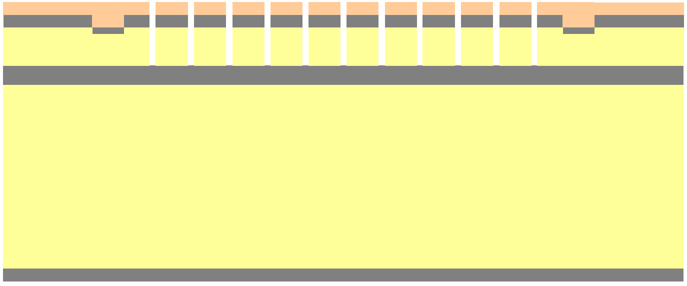

14. Removal of the photoresist.

Process described in step 6.

15. General cleanliness.

Again a cleaning process is carried out to remove all of the remains from the previous fabrication process. Process described in step 2.

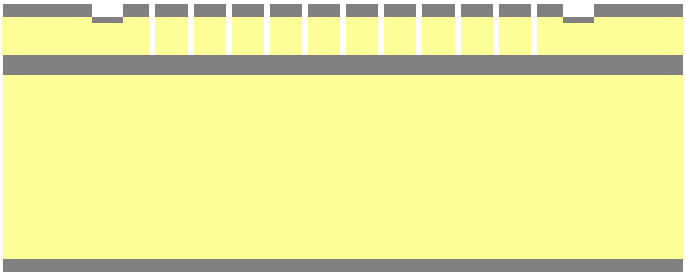

16. Polysilicon deposition.

A low pressure reactor operated between 600 and 650ºC is used to deposit polysilicon by pyrolizing silane.

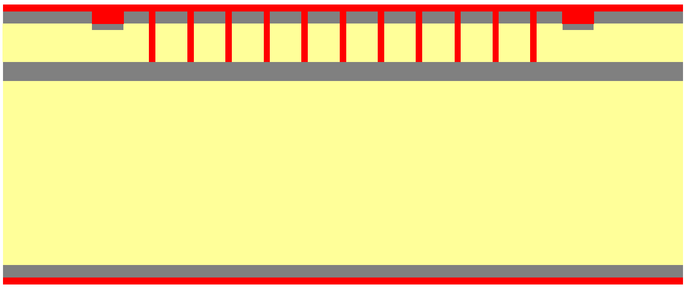

17. Photolithography.

This photoresist layer is used to define the polysilicon on the surface above the columns. Step described in 4.

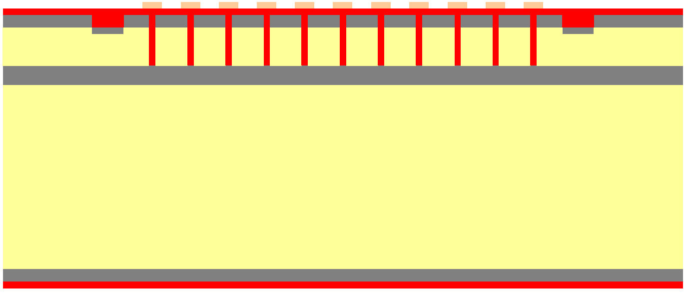

18. Reactive ion etching, top surface.

The accelerated plasma of SF_6 ions of the RIE chamber react chemically with the polysilicon of the samples, but also knock off (sputter) some polysilicon by transferring some of their kinetic energy.

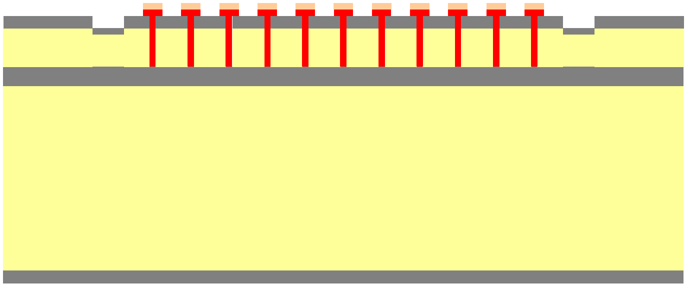

19. Removal of the photoresist.

Process described in step 6.

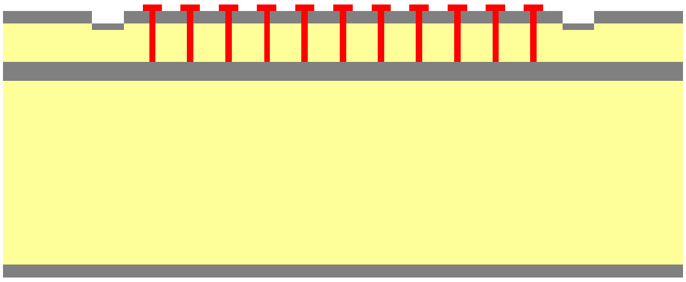

20. General cleanliness.

A general cleanliness is needed after the previous etching processes for the removal of remaining products.

21. Deposition of silicon oxide, 200 nm.

This is a plasma enhanced chemical vapor deposition (PECVD) process. It is done at 380ºC, 1 torr pressure in plasma composed by silane (SiH_4), nitrogen protoxide (N_2O) and oxygen, generated by a bias of 200V between electrodes.

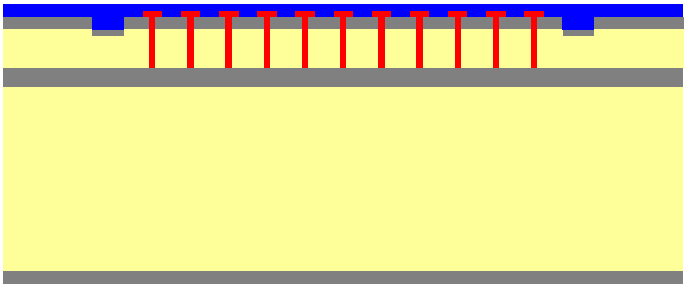

22. Deposition of silicon nitride, 350 nm.

This is a PECVD process whose aim is the passivation with silicon nitride for protection. Task carried out on the top surface.

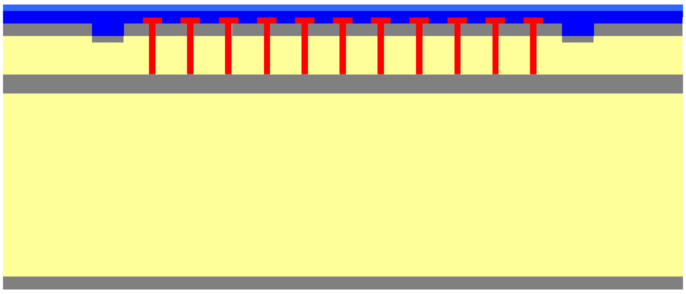

23. Deposition of silicon nitride, 350 nm.

The same PECVD process than before, whose aim is the passivation with silicon nitride for protection. Task carried out on the bottom surface.

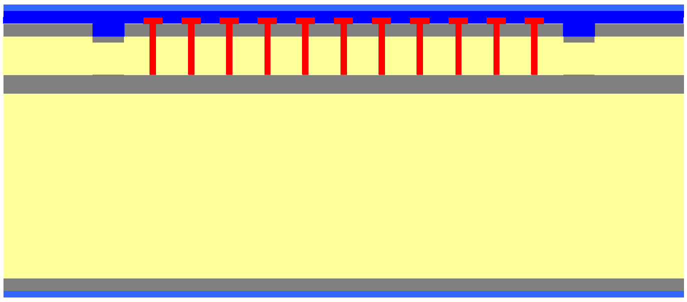

24. Double face alignment photolithography.

This photolithography is carried out on bottom surface but using the alignment marks on the top surface. This way we have the window in the photoresist (bottom) in the desired position respecting the other surface (top).

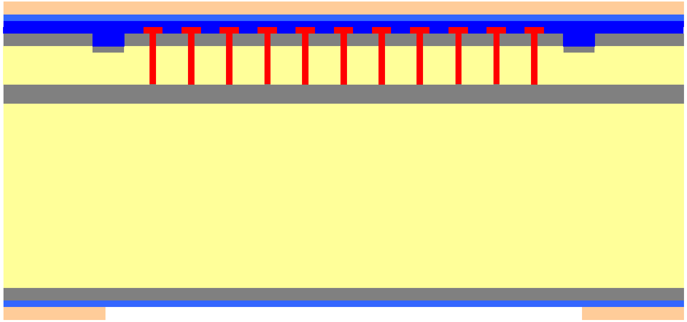

25. Dry etching.

To remove the silicon nitride (350 nm) of the bottom window a dry etching by using SF_6 is carried out, while for the silicon oxide (800nm) the active agent used is CH.

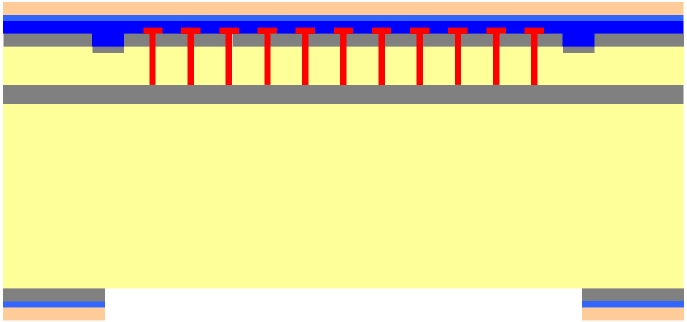

26. Removal of the photoresist.

Removal of the photoresist to let the nitride window be on the air on the bottom surface.

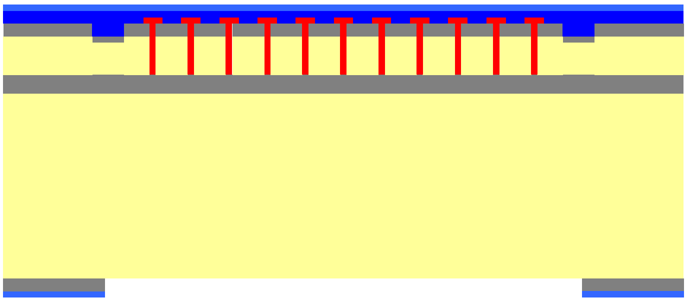

27. Wet etching of silicon (300 µm) and SOI oxide.

The final step is the thinning of the back surface of the active detector area. The thinning is done using a TMH solution which stops the etching at the oxide interface of the SOI wafer. This oxide is etched and then deposited with an ALD (atomic layer deposition) equipment obtaining a final thickness of 20 nm.

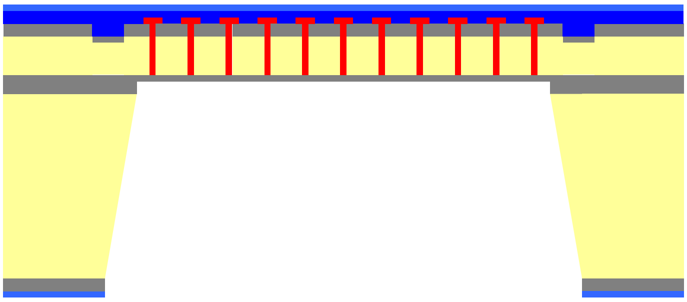

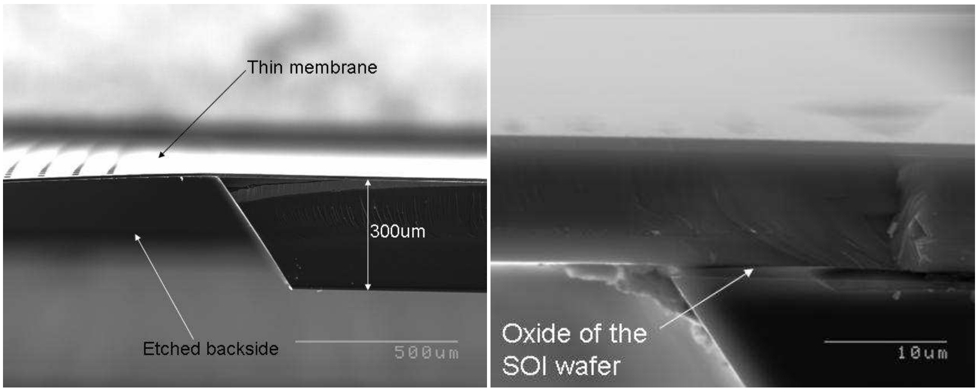

Figure 4.12: *Cross section of the membrane structure with the passing through holes (left) and close look of the junction Si-*SiO_2*-Si of the entrance window.*

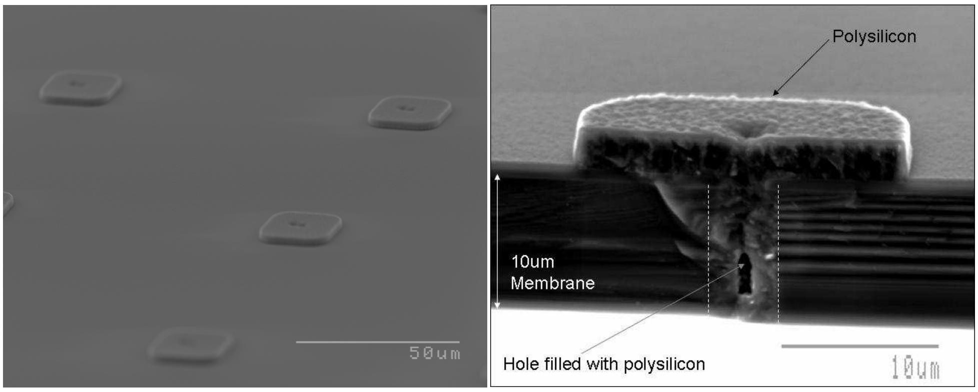

Figure 4.13: *View of the surface of the finished wafer(left) and cross section of one hole filled with posysilicon.*

The resulting membrane and a cross section of one hole filled with polysicon are shown in figure 4.12 and 4.13 respectively. The minimum thickness of the passivation layer that insures a good electrical isolation and reduces the energy lost by the incoming ions has been calculated to be on the order of 10 nm.

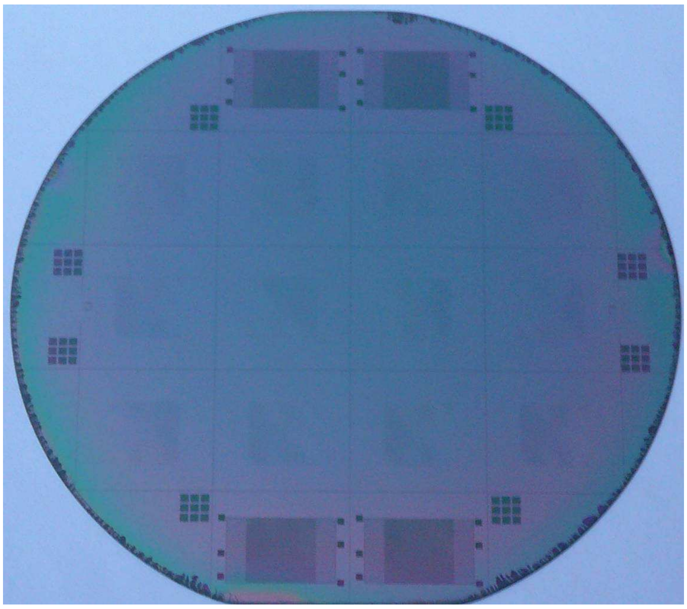

Figure 4.13: *Front view of the finished wafer with front illumination.*

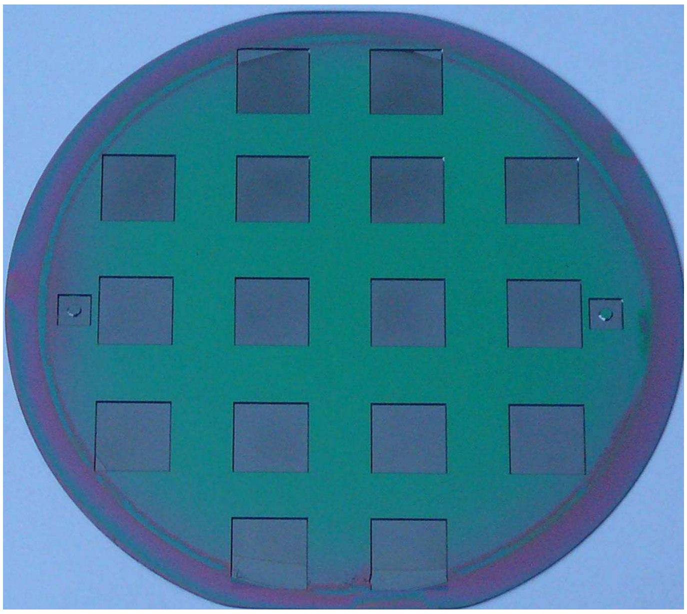

Figure 4.14: *Back view of the finished wafer with.*

Figures 4.13 and 4.14 show the final wafer with front and back illumination respectively. The squares in the wafer are the thin (10µm) membranes with 5µm holes.

4.5 Conclusions

The conceptual design of this novel type of thin silicon detectors has been presented and fabrication has been performed [67]. The electrical characteristics have been simulated and show good performance suitable for plasma diagnostic. The detector capacitance for a single cell of the

U3DTHIN is at least two orders of magnitudes than the one of a planar with the same thickness and surface area.

The first complete fabrication run finished, the detectors must be tested and their electrical behavior and charge collection measured.

4.6 Future work

This work presents the first phase in the development of a novel 3D silicon detector, such as the proper and suitable design, physical and electrical simulations, and first prototypes of fabrication.

The next step consists on electrical characterization of fabricated detectors, simulation of efficiencies of the unirradiated and irradiated detectors for different fluences, and electrical characterization and measurements on efficiencies of the irradiated detectors.

References

[1] http://lhc.web.cern.ch/lhc/

[2] http://public.web.cern.ch/public/en/LHC/LHC-en.html

[3] http://rd50.web.cern.ch/rd50/

[4] W. Kienzle. TOTEM. Total Cross Section, Elastic Scattering and Diffraction Dissociation at the LHC. CERN/LHCC 97-49 (1997).

[5] V. Avati et al. The TOTEM experiment. EPJdirect A1, 1–11 (2003).

[6] http://www.iter.org/

[7] http://lhc-machine-outreach.web.cern.ch/lhc-machine-outreach/beam.htm

[8] http://atlasexperiment.org/

[9] F. Ruggiero. LHC Upgrades (accelerator). 8th Seminar ICFA, Taegu, Korea (2005).

[10] M. Oriundo. The Roman Pots for LHC. TOT-XRP-ES-001.

[11] M. Moll. Development of Radiation Tolerant Semiconductor Detectors for the Super-LHC. Elsevier Science (2004).

[12] M. Minano. Estudio de detectores de silicio resistentes a altas dosis de radiación. Master Thesis, Universitat de Valencia (2006).

[13] G. Lutz. Semiconductor Radiation Detectors. Device Physics. Springer.

[14] M. Huhtinen. Simulation of non-ionising energy loss and defect formation in silicon. Nuclear Instruments and Methods in Physics Research A 491 (2002) 194-215.

[15] G. Lindström. Radiation damage in silicon detectors. Nuclear Instruments and Methods in Physics Research A 512 (2003) 30-43.

[16] J.R. Srour et al. Review of Displacement Damage Effects in Silicon Devices. IEEE Transactions on Nuclear Science, Vol 50, Nº 3 (2003)

[17] ASTM E722-85, ASTM E722-93 (revised), 1993.

[18] A. Vasilescu, G. Lindström, ROSE TN/2000-02 in ROSE Status Reports.

[19] G. Lindström M. Moll and E. Fretwurst Radiation hardness of silicon detectors – A challenge from high-energy physics. Nuclear Instruments and Methods in Physics Research A 426 (1999) 1.

[20] J.B. Roldán, F.J. Gámiz. Dispositivos Electrónicos. Ra-Ma. 2001.

[21] C. Fleta. Tecnología de detectores de partículas de silicio resistentes a la radiación. Thesis. Universitat Autónoma de Barcelona (2006).

[22] B.C. MacEvoy. Defect evolution in silicon detector material. IC/HEP/96-3, ROSE/TN/96-1 (1996).

[23] L. Matheson, M. Robbins, S. Watts. The effect of radiation induced defects on the performance of high resistivity silicon diodes. Nuclear Instruments and Methods in Physics Research A 377 (1996) 224-227.

[24] S.J. Watts. Radiation induced defects in silicon. 194th Meeting of the Electrochemical Society Inc., Boston, Ma, USA, November 1-6 1998.

[25] G. Davies, E. C. Lightowlers, R. C. Newman and A. S. Oates. A model for radiation damage effects in carbon-doped crystalline silicon. Semiconductor Science Technology. 2 524 (1987).

[26] G. Oehrlein, et al. Silicon-oxygen complexes containing three oxygen atoms as the dominant thermal donor species in heat-treated oxygen-containing silicon. Journal of Applied Physics. 54 179 (1983).

[27] Y. Shi, D. X. Shen, F. M. Wu, and K. J. Cheng. A numerical study of cluster center formation in neutron-irradiated silicon. Journal of Applied Physics. 67 1116 (1990).

[28] B. MacEvoy, G. Hall, K. Gill. Defect evolution in irradiated silicon detector material. Nuclear Instruments and Methods in Physics Research A 374 (1996) 12.

[29] R. A.Woolley , E. C. Lightowlers, A. K. Tipping, M. Claybourn and R. C. Newman. Defects in Semiconductors, Paris. Material Science Forum. 10-12 (1986) 929-934.

[30] E. Fretwurst et al. Survey of recent radiation damage studies at Hamburg. 3rd RD50 Workshop (2003).

[31] J. Härkönen et al. Radiation hardness of Czochralski silicon, Float Zone silicon and oxygenated Float Zone silicon studied by low

energy protons. Nuclear Instruments and Methods in Physics Research A 518 (2004) 346-348.

[32] S. Dittongo et al. Radiation hardness of different silicon materials after high-energy electron irradiation. Nuclear Instruments and Methods in Physics Research A 530 (2004) 110-116.

[33] Z. Li et al. Gamma Radiation Induced Space Charge Sign Re-inversion in Proton Irradiated High Resistivity CZ Si Detectors. 4th RD50 Workshop (2004)

[34] G. Kramberger. Effect of bias voltage on full depletion voltage measured for different materials. 9th RD50 Workshop (2006).

[35] M. Moll. Radiation damage in silicon particle detectors. Thesis. Universität Hamburg (1999).

[36] G. Pellegrini at al. Annealing Studies of magnetic Czochralski silicon radiation detectors. Nuclear Instruments and Methods in Physics Research A 552 (2005) 27–33.

[37] G. Lutz. Radiation damage in structured silicon radiation detectors. Invited talk presented at the IEEE Nuclear and Space Radiation Effects Conference. Phoenix, Arizona (2002).

[38] R.H. Ritchter et al. Strip detector design for ATLAS and HERA-B using two dimensional device simulation. Nuclear Instruments and Methods in Physics Research A 377 2-3 (1996) 412-421.

[39] T. Rohe et al. Position dependence of charge collection in prototype sensors for the CMS pixel detector. IEEE Transactions on Nuclear Science, 51(3) (2004) 1150-1157.

[40] J. Kemmer et al. United States Patent No.U.S.6.184, 562 B1 (2001).

[41] G. Casse. Performances of miniature microstrip detectors made on oxygen enriched p-type substrates after very high proton irradiation. Nuclear Instruments and Methods in Physics Research A 535 (2004) 362–365.

[42] M. Lozano et al. Ultimate limits for the radiation hardness of silicon strip detectors for SLHC. Nuclear Instruments and Methods in Physics Research A 581 (2007) 365–367.

[43] http://pcroot.cern.ch/root/

[44] M. Minano et al. Annealing studies of silicon microstrip detectors irradiated at high neutron fluences. Nuclear Instruments and Methods in Physics Research A 591 (2008) 181–183.

[45] Supply of Silicon Microstrip Sensors for the ATLAS SCT 07, Version 4.5. Technical Specifications. October

[46] ISE Integrated Systems Engineering AG. ISE TCAD version 10 manual. Zurich, Schwitzerland, 2006.

[47] G. Ruggiero.The TOTEM detectors. XIth International Conference on Elastic and Diffractive Scattering. Chateau de Blois, France, May 15 - 20, 2005.

[48] G. Ruggiero et al. Planar edgeless silicon detectors for the TOTEM experiment. IEEE Transactions on Nuclear Science, Vol. 52, No. 5, October 2005.

[49] E. Nochis, Planar edgeless detectors for the TOTEM experiment at the Large Hadron Collider, Thesis, University of Helsinki, 2006.

[50] C. DaVia, J. Hasi, C. Kenney, A. Kok, S. Parker. 3D silicon detectors—status and applications. Nuclear Instruments and Methods in Physics Research A 549 (2005) 122-125.

[51] M. Petasecca et al. Numerical Simulation of Radiation Damage Effects in p-type and n-type FZ Silicon Detectors. IEEE Transactions on Nuclear Science, Vol 33, No 5, October 2006.

[52] D. Pennicard. Simulation results from double sided and standard 3D detectors, Transactions on Nuclear Science IEEE, Volume 54, Issue 4, Part 3, Aug. 2007 Page(s):1435 – 14433.

[53] E. Nochis, V. Eremin, G. Ruggiero. Simulations of planar edgeless detectors with a current terminating structure. Elsevier Science, 13 December 2006.

[54] M. Lozano et al. Comparison of radiation hardness of p-in-n, n-in-n, and n-in-p silicon pad detectors. IEEE Trans. Nucl. Sci., Vol 52, pp. 1468-1473, 2005.

[55] G. Kramberger et al. Determination of effective trapping times for electrons and holes in irradiated silicon. Nuclear Instruments and Methods in Physics Research A 476 (2002) 645-651.

[56] E. Verbitskaya et al. Concept of double peak electric field distribution in the development of radiation hard silicon detectors. Nuclear Instruments and Methods in Physics Research A 583 (2007) 77-86.

[57] J. Uher et al. Characterization of 3D thermal neutron semiconductor detectors. Nuclear Instruments and Methods in Physics Research A 576, 2007.

[58] A. Castoldi, C. Foirini. Silicon devices for low-energy X-ray detection: comparison between the charge coupled device and semiconductor drift chamber. Nuclear Instruments and Methods in Physics Research A 397 1997.

[59] M Marisaldi et al. Silicon drift detectors coupled to CsI(Tl) scintillators forspaceborne gamma-ray detectors. Nuclear Physics B 150, 2006.

[60] M.N. Akhatar, Bashir Ahmad, Shoaib Ahmad. Low energy ion detection with the plastic scintillator NE102E. Nuclear Instruments and Methods in Physics Research B 207, 2003.

[61] G. Pellegrini et al., Technology development of 3D detectors for high-energy physics and imaging, Nuclear Instruments and Methods in Physics Research A 487 (2002) 19-26.

[62] F. Garcia et al, Novel Ultra Thin 3D Silicon Detector – Plasma Diagnostics for JET and ITER TOKAMAKS, presented at the 10th International Workshop on Radiation Imaging Detectors in Helsinki, Finland, June 29 - July 3, 2008.

[63] G. Casse et al. Performances of miniature microstrip detectors made in oxygen enriched p-type substrates after very high proton irradiation, Nuclear Instruments and Methods A 535 (2004) 362-365.

[64] M.V. Acero, J.Esteve, J.A. Plaza. Microtecnología: diario de un run. Instituto de Microelectrónica de Barcelona IMB-CNM (CSIC) 2007.

[65] S.M. Sze. Semiconductor devices. Physics and techinology. AT&T Bell Laboratories. Murray Hill, New Jersey 1985.

[66] F. García, S.S. Kozlovsky, D.V. Balin. Background Properties of CEM, MCP a nd PMT detectors at n irradiation. Preprint PNPI-2392, Gatchina, 2000, p.9.

[67] G. Pellegrini, M. Lozano, M. Ullan, R. Bates, C. Fleta, D. Pennicard, First double-sided 3-d detectors fabricated at CNM-IMB, Nuclear Instruments and Methods in Physics Research A 592 (1-2) (2008) 38-43.